AMERICAN METEOROLOGICAL SOCIETY

AMS Journals Online

Full Text View

Journal of Physical Oceanography

Observations of Overturning in the Thermocline: The Context of Ocean Mixing

Matthew H. Alford

Applied Physics Laboratory, University of Washington, Seattle, Washington

Robert Pinkel

Marine Physical Laboratory of the Scripps Institution of Oceanography, University of California, San Diego, La Jolla, California

ABSTRACT

The time sequence of events that lead to internal wave breaking and ocean turbulence is investigated. Data are obtained from depths 100–400 m with a repeat profiling CTD and a coded-pulse Doppler sonar. The instruments were deployed from R/P *FLIP* during February–March 1995 while stationed 30 km west of Point Argüello, California, as an aspect of the Marine Boundary Layer Experiment. Although the water depth at the site is 1500 m, both rms shear and diapycnal diffusivity, as inferred from the average rate and size of overturning events, increase with depth below 250 m. A deep source of wave energy is implied.

Depth–time series of 6.4-m shear S, 2-m strain ($\gamma \equiv \overline{N}^2/N^2$, where N is the buoyancy frequency), 6.4-m gradient Richardson number $\mathrm{Ri} \equiv N^2/S^2$, and 2-m "effective strain rate"

$$\frac{\partial \hat{w}}{\partial z} = \frac{1}{\gamma}\frac{\partial \gamma}{\partial t}$$

(the depth derivative of CTD-inferred vertical velocity $\hat{w}$) are obtained at 4 minute intervals over a 9-day, 100–400 m domain. The occurrence of overturns, static instabilities of vertical scale ≥ 2 m in the observed density profiles, is monitored. Data are examined in both Eulerian and isopycnal-following (semi-Lagrangian) reference frames.

Over two thousand overturns are detected and mapped relative to the

Options:
- Create Reference
- Email this Article
- Add to MyArchive
- Search AMS Glossary

Search CrossRef for:
- Articles Citing This Article

Search Google Scholar for:
- Matthew H. Alford

background shear, strain, Ri, and strain rate fields. Correspondence between low values of 6.4-m Ri and overturns is indeed significant. However, 2-m strain and effective strain rate appear to be better indices of overturning: $\gamma \geq 2$ in 60% of all overturning events, and $|\partial \hat{W}/\partial z|$ is greater than average in 80% of overturns.

• Robert Pinkel

Depth–time maps of effective strain rate show wavelike features on vertical scales 5–20 m, which extend coherently across isopycnal surfaces. Time series of depth-averaged $\partial \hat{W}/\partial z$ variance (expressed as a dissipation rate), and depth-averaged dissipation rate ε_T, estimated from observed overturning scales are highly correlated. Time-mean $\overline{\varepsilon_T} = 8.6 \times 10^{-9}$ W kg^{-1}, implying an eddy diffusivity $\overline{K_\rho} = 0.89 \times 10^{-4}$ m^2 s^{-1}. Mean dissipation rate and diffusivity computed from 10-m shear display comparable magnitude ($\overline{\varepsilon_{1w}} = 6.8 \times 10^{-9}$ W kg^{-1}, $\overline{K_\rho} = 0.70 \times 10^{-4}$ m^2 s^{-1}) and similar dependence upon mean stratification and shear to the overturn-inferred quantities. It is suggested that the overturns seen at this site result from breaking of these high $\partial \hat{W}/\partial z$ waves.

1. Introduction

a. Focus

Ocean mixing in double-diffusively stable regions of the thermocline is thought to be accomplished through dynamic instability of finescale motions. Gravitationally unstable regions ("overturns") are produced, which subsequently collapse, dissipating mechanical energy and diffusing scalar quantities. The vertical fluxes produced by this mixing are of importance in maintaining global balances. Proper parameterization of dissipation rate in general oceanic environments requires an understanding of the governing factors. With this as a goal, we present simultaneous observations of overturns and the finescale conditions that accompany them. The issue of flow context is central.

Overturns can result from Kelvin–Helmholtz (K–H) or shear instability (Miles 1961; Howard 1961), the convective instability of internal waves (Orlanski and Bryan 1969), and several other mechanisms. The objective of this study is to identify the processes that lead to instability. We focus on the phenomenon of (meter scale) overturning rather than the measurement of (centimeter scale) microstructure. Observations of overturning and of microstructure offer complementary views of the mixing process. To oversimplify, we view the overturns as an early phase of the instability and the microstructure as the aftermath. (Microconductivity data from this experiment are analyzed in a companion paper.)

Overturns are monitored over a 300-m vertical extent for nine days in March 1995 in a strongly sheared, coastal environment. Depth–time fields of 6.4-m Ri, 2-m strain γ, and a quantity termed the 2-m "effective strain rate" $\partial \hat{W}/\partial z$ are also measured with the overall aim of determining the relationship between these finescale quantities and overturning.

The paper is organized as follows. Section 2 provides an overview of conditions and observations made during the experiment, as well as a description of the methods and definitions used. Section 3 focuses on depth–time maps of Ri, γ, and $\partial \hat{W}/\partial z$ for a representative 12-h period. Locations and times of overturns are overplotted, allowing visual determination of the finescale conditions that accompany them. In section 4, probability density functions of these quantities are produced, using the complete dataset as well as subsets of the data where overturning is observed. In addition, related PDFs are computed using data sampled just before, and just after, overturns. This statistical approach corroborates the qualitative conclusions drawn from section 3. Section 5 examines time series of several indirect estimates of depth-averaged dissipation rate. Section 6 discusses the dependence of overturning, and resulting mixing, upon instantaneous and mean stratification. The relative contributions to total mixing from overturns of varying size and background stratification are presented in section 7. Section 8 is a summary. Conclusions are presented in section 9.

b. Background

A pioneering study of mixing and its finescale context was conducted by Gregg et al. (1986), who tracked a persistent mixing patch, 5–10 m thick, for several days. It appeared to be associated with a near-inertial feature. The patch was centered, during most of its lifetime, on the velocity maximum of the feature, not the shear maximum. Gregg et al. (1986) suggested that the near-inertial wave provided a preferential site for instability of smaller-scale internal waves.

Marmorino et al. (1987), using Doppler sonar and towed thermistor chains, monitored meter-scale temperature fluctuations as well as larger-scale variations (7–50 m) in shear and Richardson number. They observed a number of regions of intense temperature fluctuation similar to the one observed by Gregg et al. (1986). These also had 5–10 m thickness and existed within a near-inertial wave packet. Within the patches 1–3 m overturns were observed. The patches were associated

with high shear and with values of 7-m Ri lower than one.

In addition to the near-inertial groups, Marmorino et al. (1987) observed small-scale internal wave groups (e.g., their Fig. 6a). The groups had vertical extent 5–8 m and horizontal wavelength 20–30 m. One-meter temperature inversions observed within the groups were interpreted as evidence of wave breaking. Observed 7-m Ri in this region was greater than unity.

Hebert et al. (1992) observed a 22-m overturn above the core of the equatorial undercurrent. Using towed thermistor data, they showed that it was associated with low Ri and high internal wave strain $\gamma \equiv \overline{N^2}/N^2$, where

$$N = \sqrt{\frac{g}{\rho} \frac{\partial \rho}{\partial z}}$$

is the buoyancy frequency (their Figs. 2a and 3c). A packet of high frequency ($\omega \geq N/2$), high vertical wavenumber ($m \geq 1/100$ cpm) internal waves was also present. High correlations were observed between dissipation rate and the presence of these waves (Moum et al. 1992). The authors concluded that instability associated with the waves generated the overturn. However, they were unable to determine the specific instability mechanism responsible.

In parallel with these observations, theoretical studies by Henyey et al. (1986) and Broutman and Young (1986) have explored the processes that transfer energy from the larger-scale flows to breaking scales. The vertical scale of internal waves can be reduced through refraction by the "background" flows of larger-scale waves (Henyey et al. 1986; Broutman and Young 1986). Their Eikonal approach involves injecting "test waves" into a Garrett and Munk (1975) background wavefield (Henyey et al. 1986) or into a near-inertial wavefield (Broutman and Young 1986), and tracking the resulting changes in wavenumber and frequency.

It has thus far been difficult to resolve small-scale internal waves in the ocean and to verify whether this mechanism is the dominant cascade process. However, the Eikonal approach provides an important intellectual context for this work. Observations are here presented of small-scale propagating disturbances with some of the same characteristics as these "test waves."

2. Observations and methods

a. Experiment

An eight-beam Doppler sonar system and a repeat-profiling CTD (Fig. 1) were operated from the Research Platform *FLIP* during the first leg of the Marine Boundary Layer Experiment (MBL I, Feb–Mar 1995). The experiment was sited approximately 30 km west of Point Argüello, California, in 1.5 km of water (Fig. 2). *FLIP* was secured with a one-point mooring during the first part of the experiment (Fig. 2). Five days before the end of the experiment, on 6 March (yearday 66), the mooring was released and *FLIP* drifted freely toward the northwest.

The 9-day mean buoyancy frequency profile (Fig. 3 , heavy line) peaks at 7 cph at 30 m, dropping approximately exponentially to 2 cph at 400 m.

Mean velocities relative to *FLIP* are computed over the moored portion (yearday 59–66) of the experiment (Fig. 4 , heavy solid line), the drifting portion (yearday 66–68, heavy dashed line), and the 12-h period from yearday 67.5–68 (light black line). The moored averages reflect the presence of a persistent westward "jetlike" flow: at times, observed surface currents during the experiment exceed 1 m s^{-1}. While drifting, *FLIP* approximately follows the depth-mean current from 0 to 90 m (Smith 1998). During this period, currents relative to *FLIP* from 100 to 400 m are smaller than during the moored period, but still appreciable (10 cm s^{-1}).

MBL I is an energetic, coastal site. Strong shears, large baroclinic tidal displacements, and frequent overturns are observed, making it an ideal location for a mixing study. An awareness of the differences between MBL I and more typical conditions is, however, essential. To illustrate, the depth dependence of shear squared and the tidal displacements are discussed here briefly.

Garrett and Munk (1972, 1975; henceforth GM75) synthesized numerous observations to provide a characterization of "typical" open ocean conditions. To compare MBL I shears with GM75 conditions, 6.4-m $\overline{S^2}$ is plotted as a function of mean buoyancy frequency $\overline{N}$ (Fig. 5). Profiles are multiplied by 1/(0.6) to account for biasing due to horizontal

separation of the sonar beams (appendix A) and corrected for attenuation by the first-difference operator. At all depths, $\overline{S^2}(\overline{N})$ is significantly above GM levels (dotted line). However, observed $\overline{S^2}(\overline{N}) \sim \overline{N}^2$ for $\overline{N} \geq 2.75$ cph (depth $\lesssim 250$ m). Below this, shear increases with depth (decreasing $\overline{N}$), departing from the GM75 standard.

Doppler sonar records often suffer from increased noise at great range as the strength of the returned signal falls. If the observed deep elevated shear were due to instrument noise with a white frequency spectrum, the shear variance should decrease by a factor of 6 and 30 as the time-averaging is increased from 4 min (right) to 24 min (middle) to 2 h (left). The decrease is, in fact, much less, indicating that the frequency spectrum of the observed shear is red, not typical of noise. Visual examination of individual velocity profiles (Fig. 9 ⊙) provides additional confidence that noise is not dominant. Increasing $\overline{S^2}$ with depth below 250 m is a robust feature of the MBL I site, presumably due to bottom-generated motions.

In addition, baroclinic tidal activity is much stronger in MBL I than typically seen in the open ocean. During the spring tide of early March (yearday 59–62, Fig. 6 ⊙), 40-m vertical displacement of isopycnals is observed at depths of 100–200 m. Heightened potential energy due to the displacements (black contours) is associated with a discrete tidal ray emanating from nearby topography.

b. CTD observations

The CTD, a modified Sea-Bird Instruments SBE-9, profiles the upper 415 m of the water column every 4 minutes. The fall rate of the instruments is approximately 3.6 m s^{-1}. At this rate it is not necessary to pump the conductivity cell to assure adequate flushing. Data are sampled at 24 Hz, providing a measurement every 15 cm. Only the downcast of each drop is used for analysis; during the upcast the sensors are in the wake of the package. A Macintosh computer controls the CTD winch, reads and stores the data, and displays them in real time. An external clock ensures that the profiles are synchronized to the sonar, as well as to other onboard sensors.

To reduce the effects of salinity spiking, the cross-spectrum between conductivity and temperature is estimated, using data from a region of near-uniform salinity. The magnitude and phase of conductivity are then altered to match those of temperature. The data are corrected for effects of the thermal inertia of the conductivity cell, as described in Lueck and Picklo (1990) and Morison et al. (1994). Temperature and conductivity are then low-pass filtered with a 2-m cutoff, and salinity and density are computed. The matching technique is described in more detail in Anderson (1993) and Sherman (1989).

c. Overturns

The CTD data are used to form time–depth series of density, buoyancy frequency, isopycnal depth, strain, and effective strain rate as described below. They also determine the locations of overturning events.

The Thorpe scale L_T (Thorpe 1977) is a useful indicator of both the location and vertical extent of overturning regions. Within observed density inversions, data are sorted to reestablish a monotonically increasing profile. The Thorpe displacement Th(z) is the vertical distance each parcel of water must be moved to restore it to a stable position in the water column (Fig. 7 ⊙). Thus Th is zero except in the vicinity of density inversions. There, it is an objective measure of vertical excursions within the overturn. Other useful overturn statistics include the maximum displacement L_{max} and the patch size L_P, defined as the region over which Σ (Th) = 0 (Seim and Gregg 1994).

In practice, it is often difficult to determine whether observed density inversions are in fact statically unstable overturns. There are two main challenges. First, random noise in the temperature and conductivity sensors can introduce unphysical inversions. These might appear in low-temperature-gradient regions, where small sensor-induced fluctuations are comparable in magnitude to the true background gradient. Second, salinity spiking can create spurious inversions in density. Spiking can be detected either by examining water-mass characteristics in the immediate vicinity of the inversion, and insisting on a tight T–S relation (Galbraith and Kelley 1996), or by requiring that Thorpe displacements be nonzero in both temperature and density (Peters et al. 1995).

To maximize confidence in our determination of overturning, temperature, conductivity, and density profiles are independently sorted and Thorpe displacements computed for each. Only regions for which the conductivity- and density-based Thorpe displacements are comparable to the temperature-based Thorpe displacement are classified "overturns." These regions are characterized using the temperature-based Thorpe displacement, rather than the density-based one, to exclude noise introduced in the density calculation. By requiring that inversions be present in both temperature and conductivity records, we minimize the influence of random noise in the sensors. In fact, nearly every observed inversion in temperature is accompanied by one in conductivity. Insisting that both temperature and density invert ensures neither lateral intrusions nor salinity spiking contaminates the overturn record. Given this cautious approach, we may not have caught all of the overturns

but are confident that we have not introduced spurious ones.

A sample (large) overturn, which passed these tests, is shown in Fig. 7 ⊙. Unfiltered (15 cm) conductivity and temperature are converted to equivalent densities and plotted on the same axis as density. The sorted density profile is overplotted. Calculated Thorpe displacements are shown to the right. Despite the higher resolution of the unsmoothed temperature and conductivity relative to density, all three profiles show similar Thorpe signatures.

Stable (salinity compensated) temperature inversions are common at the MBL site, particularly above 200 m. We restrict quantitative studies to the range 200–350 m to minimize concerns of intrusive contamination.

To produce depth–time maps of overturning, profiles of Th are initially formed. A list of time–depth pairs is then created, documenting each region in which the maximum Thorpe displacement L_{max} exceeds 2 m. In all, 2227 overturns with L_{max} ≥ 2 m were detected over the 9-day period (yearday 59–68), between 200 and 350 m. These occupy 3.06% of the sampled water column (Table 1 ⊙). During the 12-h period (yearday 67.5–68.0) highlighted in this work, 330 overturns with L_{max} ≥ 2 m were found (Table 2 ⊙). They occupy 2.96% of the water column.

The probability density of L_T for the 2227 overturns is presented in Fig. 8 ⊙. The PDF falls off for L_T ≲ 1.5 m, reflecting our minimum size cutoff. For L_T ≥ 1.5 m, the distribution is consistent with the tail of a lognormal distribution (dashed line), with $\sigma_{\log_{10}L_T}$ = 0.37, $\overline{\log_{10}L_T}$ = −0.1. Lognormal distributions of L_T are typically observed (e.g., Wijesekera et al. 1993; Moum et al. 1992).

d. Sonar observations

The Doppler sonar, designed and constructed at the Marine Physical Laboratory of Scripps, was mounted on the stern of *FLIP* at approximately 87-m depth (Fig. 1 ⊙). It consists of four upward-looking (170 kHz) and four downward-looking (140 kHz) beams directed 30° from vertical. Only the downward-looking portion of the sonar data is used here. A repeat sequence code (Pinkel and Smith 1992) consisting of four repeats of a 7-bit Barker code is transmitted. The bandwidth of the transmitted code is 16.6 kHz. Vertical resolution is 3.2 m (however, data are sampled every 1.6 m). Transmissions are made every 1 s, and estimates recorded every minute. To improve precision and to enable integration with CTD data, 4-min averages are subsequently formed. These are aligned in time with the downward section of each CTD profile. The rms precision of these 4-min averages, estimated from frequency spectra, is 1.1 cm s^{-1}. The usable range of depths sampled by the downward-looking sonar is 100–500 m. Horizontal velocity estimates are computed by averaging back-to-back beam velocities. Shear magnitude, S, is computed by differencing velocities over 6.4 m and then smoothing with a 6.4-m convolution filter.

A sample of full (3.2 m)-resolution velocity data is displayed in Fig. 9 ⊙. Twenty profiles of zonal velocity spanning 80 min near yearday 67.9 are plotted, offset by 5 cm s^{-1}. Note the reproducibility of small-scale velocity features from profile to profile.

The high quality of the MBL sonar enables the present examination of finescale Ri. Still, two aspects of the sonar affect S^2 (and therefore Ri) estimates. The horizontal separation of the beams biases S^2 low since shear on horizontal scales comparable to the beam separation is underrepresented: Instrument noise biases S^2 high. These competing effects are discussed in appendix A.

e. Finescale quantities

Estimates of the 6.4-m Richardson number are formed from the combined CTD and sonar data. Profiles of buoyancy frequency N are formed by differencing the sorted density profiles, then smoothing with a 6.4-m Butterworth filter. This procedure ensures that the two constituents of Ri have similar bandwidth. Variations in N are comparable to those in S in producing 6.4-m Ri fluctuations.

We wish to monitor fluctuations in finescale quantities in both Eulerian and isopycnal following frames. The Eulerian time series of a thermocline variable reflects temporal and spatial variability; that is,

$$\frac{\partial \theta}{\partial t} = \frac{D\theta}{Dt} - \mathbf{u} \cdot \nabla \theta.$$

When $\nabla\theta$ has finescale irregularities, the time series is termed "fine-structure contaminated." With a continuous depth–time view, we can alter the concept of an Eulerian time series to avoid "contamination." Specifically, we define the Eulerian time fluctuation of a variable at depth z_o relative to its time mean, where the mean is taken along the isopycnal, which is passing through z_o at that instant.

As an example, consider an Eulerian temperature record under this definition:

$$\hat{T}_{\text{Eul}}(t,\ z) \equiv \frac{T(t,\ z)}{\overline{T(\rho(t,\ z))}}, \qquad (1)$$

where $\hat{T}_{\text{Eul}}$ indicates whether the various isopycnal surfaces passing through z_o are warmer or colder than their respective long-term average values. In the absense of lateral T–S variability, mixing, and radiative transport an Eulerian temperature record is constant. The signature of vertical advection is absent.

In like manner, we consider the anomaly in strain

$$\gamma_{\text{Eul}}(t,\ z) \equiv \left[\frac{N^2(t,\ z)}{\overline{N}^2(\rho(t,\ z))}\right]^{-1} \qquad (2)$$

and squared shear

$$\hat{S}^2_{\text{Eul}}(t,\ z) \equiv \frac{S^2(t,\ z)}{\overline{S^2(\rho(t,\ z))}}. \qquad (3)$$

The Eulerian Richardson number is simply related to the strain and shear anomalies:

$$\text{Ri}_{\text{Eul}} \equiv \frac{N^2}{S^2} \equiv \frac{\overline{N}^2(\rho(t,\ z))}{\overline{S^2(\rho(t,\ z))}} \gamma_{\text{Eul}}^{-1}\hat{S}_{\text{Eul}}^{-2}. \qquad (4)$$

It is also instructive to examine time variability in a semi-Lagrangian (isopycnal following, s-L) reference frame. The s-L frame is established by a set of reference isopycnals, $\{\rho_i\}$, whose mean depths are separated by 1 m. The depth $z(t,\ \rho_i)$, and displacement $\eta(t,\ \rho_i) \equiv z(t,\ \rho_i) - \overline{z}(\rho_i)$, of each isopycnal are computed from each density profile (after sorting to remove inversions) by linear interpolation. Observations are expressed in an s-L frame by linear interpolation of the Eulerian data to the depths of the specific reference isopycnals.

It is convenient to define s-L strain slightly differently than in an Eulerian frame (Pinkel et al. 1991). Between any two time series of isopycnal depth $z(t,\ \rho_i)$ and $z(t,\ \rho_j)$, the normalized depth difference is given by

$$\gamma(t,\ \overline{z}) \equiv \gamma_{ij}(t) = \frac{\Delta z_{ij}(t)}{\overline{\Delta z}} = \frac{z(t,\ \rho_i) - z(t,\ \rho_j)}{\overline{\Delta z}}, \qquad (5)$$

where $\overline{z}$ is the mean depth of the pair and $\overline{\Delta z}$ is the mean separation. The finite difference strain is defined in terms of the normalized isopycnal separation:

$$\hat{\gamma}_{ij}(t) = \gamma_{ij} - 1 = \frac{1}{\overline{\Delta z}}(\Delta z_{ij}(t) - \overline{\Delta z}). \qquad (6)$$

Positive values of strain (normalized isopycnal separation greater than one) refer to isopycnals farther apart than average.

An "effective strain rate" can be defined as

$$\frac{\partial z}{} \qquad \Delta z \qquad \Delta z \qquad \frac{\gamma\;\partial t}{}$$

To estimate this quantity, strain observations are differenced in time and divided by the normalized separation. Precision of γ and $\partial\hat{w}/\partial z$ estimates is discussed in appendix B.

The lateral advection of horizontal structure complicates interpretation of this strain rate. In fact,

$$\frac{\partial\hat{w}}{\partial z} = \frac{\partial w}{\partial z} + \partial/\partial z(\mathbf{u}\cdot\boldsymbol{\nabla}_H\eta). \qquad (8)$$

Specific acknowledgment of the advective presence in these data distinguishes our "effective strain rate" from the true "vertical divergence" $\partial w/\partial z$ as considered in Sun and Kunze (1999), for example.

3. Depth–time maps

a. Eulerian maps

Representative 12-h depth–time series of Eulerian 2-m strain γ_{Eul}, 6.4-m shear squared anomaly $\hat{S}^2_{Eul}$, and 6.4-m Ri Ri_{Eul} are presented in Fig. 10 ⭕. Twenty-three such 12-h periods have been examined. One hundred and eighty 4-min profiles compose each 12-h map.

Two-meter Eulerian γ_{Eul} (Fig. 10a ⭕) represents the distortion of the water column by passing waves. (It is also affected to a smaller degree by lateral intrusions—see appendix C.) By and large, strain features advect vertically with the displacement field. However, some cross-isopycnal migration is seen (this aspect of the strain field will be seen more clearly in the s-L view). Notice the tendency of overturns (yellow–green dots) to lie in regions of high strain, low N.

The 6.4-m $\hat{S}^2_{Eul}$ is characterized by "layers" of several hours duration (Fig. 10b ⭕). These are advected vertically by the isopycnal displacement field, as observed by Anderson (1993). High frequency features are reproduced in the shear and displacement fields (e.g., the "wiggles" at yearday 67.63–67.65, 150 m).

Contributions to Ri may be examined separately in Figs. 10a and 10b ⭕; jointly in Fig. 10c ⭕. Layers of low Ri advect vertically with time with an apparent (advection affected) timescale of a few hours. By and large, these layers follow isopycnal surfaces. However, there are notable exceptions, which will be more apparent in the close-ups and s-L maps, which follow.

Many overturns (black dots) lie in regions of low 6.4-m Ri (e.g., yearday 67.93, 350 m, yearday 67.93, 350 m and yearday 67.94, 300 m). Larger-scale internal waves vertically advect the latter region and associated overturns. The large overturning region beginning at yearday 67.75, 375 m is centered on a low Ri, high shear layer but moves relative to it.

Some layers of 6.4-m Ri remain low for hours without any observed 2-m overturning (e.g., yearday 67.8–67.9, 350 m). The Richardson number Ri must remain subcritical long enough for instability to develop, a time of order $4/(|S| - 2N)$ (Hazel 1972). Therefore a one-to-one relationship between low Ri and overturning is not expected. For example, Kunze et al. (1990) noted a lack of 1-m overturns in unstable 1-m Ri regions. But the lack of 2-m overturns in low 6.4-m Ri regions is surprising. Assuming that there is active overturning, which we do not resolve, a significant separation between the scale of the unstable Ri and that of the resulting instability is implied. Alternately, $Ri \lesssim Ri_c$ (where Ri_c is a critical Richardson number) may be necessary, but not sufficient, for instability, as suggested by linear theory (Miles 1961; Howard 1961).

Seventy-four percent of overturns lie in regions of 6.4-m Ri ≥ 1, 50% where 6.4-m Ri ≥ 2. Regions at (yearday 67.75, 150 m), (yearday 67.95, 160 m), and (yearday 67.73, 340 m) are examples. Many such overturns lie in regions of either high strain or high effective strain rate magnitude (described below).

Recall that shear variance estimates (on which 6.4-m Ri is based) are increased by instrument noise and decreased by the finite beam separation of the sonar (appendix A). Our 6.4-m Ri estimates might be large by as much as a factor of 1/(0.6) relative to a "true" 6.4-m Ri estimate.

In addition, vertical resolution is a concern: Ri decreases with decreasing vertical scale (e.g., Kunze et al. 1990). Assuming a "canonical" shear spectrum white out to vertical wavenumber $m = 0.1$ cpm and falling off as m^{-1} thereafter (Gargett et al. 1981), 6.4-m S^2 is only 55% of 2-m S^2. Nevertheless, the observed large-scale patterns are intriguing. Is

(unresolved) shear between 6.4 m and 2 m sufficient to trigger 2-m overturns? The observations of extended regions of low 6.4-m Ri with no 2-m overturning, by contrast, are robust with respect to instrument concerns.

Apparent time variability in Fig. 10 ⊙ and subsequent figures is due to true temporal modulation, mixing, and the advection of features past *FLIP*. Relative currents are 20 cm s^{-1} toward the south-southwest during this period (Fig. 4 ⊙). In the absense of intrinsic temporal changes, an observed hour-long feature would correspond to a 720-m-long structure drifting past at 20 cm s^{-1}. Attempts in later sections (3d and 4b) to assess the relative contributions of intrinsic and advective variability suggest that neither can be ignored.

b. Case studies of instabilities

It is of value to examine individual overturning events in detail. In Fig. 11 ⊙, we present close-ups in depth ($\lesssim$ 50 m) and time ($\lesssim$ 3 h) centered around three different overturning events seen in Fig. 10 ⊙.

Figure 11a ⊙ shows a series of overturning events associated with low 6.4-m Ri. Shear is high in this region, as evident from Fig. 10b ⊙. In addition, the buoyancy frequency is low, as indicated by a larger than average spacing between isopycnals. The region is sandwiched between higher gradient regions above and below. The feature crosses five isopycnals (moving toward less dense water) over the 3-h period. It is also advected vertically with the background flow. Intermittent overturning is approximately centered on the shear maximum. We interpret Fig. 11a ⊙ as a "classic" shear instability, caught in the act.

Figure 11b ⊙ depicts a second event, where 6.4-m Ri is not uniformly low (the color scale has been extended so that white indicates Ri $\geq$ 2, instead of Ri $\geq$ 1 as in Figs. 11a and 11c ⊙). Scale differences (6.4 m for Ri, 2 m for overturns) and/or beam separation effects (section a of appendix A) may be responsible for the poor correspondence. However, the event is also associated with the passage of a strain feature across these isopycnals, as seen by the large isopycnal separation. High-wavenumber, high-frequency motions make the isopycnals appear "jittery" in this region. These motions will be explored in detail in section 3d. Overturning ceases when the feature propagates (or is advected) away.

A third example of an instability event is presented in Fig. 11c ⊙. It is associated with low 6.4-m Ri, as in Fig. 11a ⊙, and with the passage of a small-scale disturbance, as in Fig. 11b ⊙. Very large overturns are colocated with a high strain feature, which "peels off" isopycnals from above as it migrates vertically. Reminiscent of a spilling surface wave, overturning follows the wave feature as it migrates upward.

c. Semi-Lagrangian maps

In Fig. 12 ⊙, semi-Lagrangian maps of strain, shear squared anomaly, and Ri are presented from the same time and depth range as the Eulerian fields of Fig. 10 ⊙. Each map has been averaged over 24 min (six profiles) in time prior to plotting (longer time averaging is possible in the s-L frame since smearing of features by vertical advection is avoided). The ordinate is not depth, but rather the isopycnal whose mean depth is indicated. Vertical excursions on a s-L plot imply cross-isopycnal migration, while horizontal variations indicate change at fixed density.

Contours surrounding regions of 6.4-m Ri $\leq$ 1 have been plotted in Figs. 12a and 12b ⊙. Low-Ri regions are formed by both high shear and low strain; ignoring variations in either constituent is not justifiable.

The 2-m $\gamma_{s\text{-}L}$ features (Fig. 12a ⊙) slowly migrate across isopycnal surfaces; e.g., at (yearday 67.77, 330 m) and (yearday 67.52, 250 m). They persist for several hours on average. Lateral advection affects the perceived cross-iospycnal migration: observed vertical excursions can represent true propagation or the sampling of spatially tilted features as they drift past.

Overturns, marked with yellow–green spots, demonstrate a clear tendency to lie in regions of high strain. Persistent, high strain features that exhibit overturning are reminiscent of the low-gradient, high-dissipation "patches" observed by Gregg et al. (1986) and by Marmorino et al. (1987). Relative to 6.4-m shear (Fig. 10b ⊙) and 6.4-m Ri (Fig. 10c ⊙), changing (propagating) strain is often the best indicator of overturn locations.

d. Effective strain rate

The effective strain rate, $\partial \hat{W}/\partial z$ (Fig. 13a ⊙), involves both the depth and time derivatives of isopycnal displacement, emphasizing higher-frequency, higher-wavenumber constituents in the resolved field. In the absence of horizontal advection, it is equivalent to the "vertical divergence" $\partial w/\partial z$ [Eq. (8)], which appears in the ray-tracing equation governing the time rate of change of the vertical wavenumber of a Henyey/Broutman "test wave" (Sun and Kunze 1999).

Imprecision in density estimates introduces rms $|\partial\hat{W}/\partial z|_{\text{noise}} = 3.2 \times 10^{-4}$ s^{-1} in our estimates (appendix B). The color scale of Fig. 13 ⊙ is such that strong features are well above the noise level.

Wavelike motions are seen in the $\partial\hat{W}/\partial z$ field. Anticipated horizontal phase speeds (0.5–5 cm s^{-1}, appendix D) are lower than typical advective velocities (Fig. 4 ⊙, 20 cm s^{-1}). Sloping features may therefore represent the advection of spatially slanted wave crests, in addition to true vertical propagation.

To focus on the wavelike aspects of the $\partial\hat{W}/\partial z$ field, components of downward-propagating (Fig. 13b ⊙) and upward-propagating phase (Fig. 13c ⊙) are separated. These are formed by two-dimensional Fourier transform filtering of the depth–time series in Fig. 13a ⊙.

Clear "groups," localized regions of large amplitude, may be seen in both upward and downward fields. Notice the presence of upward-traveling groups, with downward-traveling phases (consistent with linear internal wave propagation): for example, Fig. 13b ⊙ (yearday 67.73, 300 m), (yearday 67.53, 240 m), and (yearday 67.57, 170 m). Also common, however, are regions where group and phase are both up (e.g., yearday 67.72, 200 m) or both down (e.g., yearday 67.73, 250 m). These apparent nonpropagating features are consistent with the lateral advection of internal wave groups.

Other interpretations are of course possible. However, if the observed $\partial\hat{W}/\partial z$ features result, for example, from the advection of quasi-permanent density structure, it is hard to account for the regular crest/trough patterns, groupiness and presence of up/down features in the same region. If the signals do indeed represent waves, what can be conjectured about their intrinsic frequency and magnitude?

The intrinsic frequency ω_{int} is difficult to determine, given the Doppler shifting of the waves by background currents and larger waves (Doppler shifting due to vertical motions is absent in a s-L frame). Still, simple estimates of ω_{int} and horizontal wavenumber k may be made assuming a linear internal wave dispersion relation and advection by observed horizontal currents (appendix D). In a current of 20 cm s^{-1}, a typical wave of vertical wavenumber 0.08 cpm (12 m) and observed frequency 4 cph (like the feature at yearday 67.73, 300 m) would have ω_{int} near 0.14 cph (7 h timescale) and k near 5.7×10^{-3} cpm (180-m wavelength), for a variety of propagation directions relative to the current. Advection can shift such waves from intrinsic timescales of hours to observed frequencies near N and higher. Uncertainties in velocity and encounter angle strongly affect these estimates.

It is also instructive to consider the magnitude of fluctuations that results from a single internal wave with displacement $\eta = a \sin(kx + mz - \omega_{\text{int}} t)$; k and m are horizontal and vertical wavenumbers, and ω_{int} is the intrinsic frequency. Then, $|\partial\hat{W}/\partial z| = am\omega_{\text{int}}$. To prevent isopycnals from crossing, $am = |\hat{\gamma}| \leqslant 1$. Here $\omega \leqslant N$ implies $|\partial\hat{W}/\partial z| \leqslant N = 5 \times 10^{-3}$ s^{-1} (3 cph), representing an upper bound on single-wave "intrinsic" contributions to $\partial\hat{W}/\partial z$. Observed values are in this range (Fig. 13 ⊙, Figs. 19–20 ⊙). On the other hand, the same wave swept past *FLIP* at velocity U would produce $|\partial\hat{W}/\partial z|_{\text{adv}}$ [the second term on the rhs of Eq. (8)] $= Ukma$. Taking $U = 20$ cm s^{-1} and $k = 1/(300$ m), $|\partial\hat{W}/\partial z|_{\text{adv}} \leqslant 4 \times 10^{-3}$ s^{-1}—the same order as the intrinsic term.

Based on these simplistic considerations, the observed $\partial\hat{W}/\partial z$ features appear consistent with Doppler-shifted internal waves of intermediate frequencies. Still, their short duration and limited vertical propagation range suggest that they are significantly nonlinear, violating the assumptions of the intrinsic frequency calculation. A more detailed study of the dynamics of these waves is clearly called for and will be the subject of a future paper.

Whatever their nature, overturns are much more likely to occur in regions of high $|\partial\hat{W}/\partial z|$ (Fig. 14 ⊙). Here the envelopes of the small-scale wave packets are highlighted. For example, the instability event given in close-up (Fig. 11c ⊙) appears on this plot as a feature that begins at (yearday 67.5, isopycnal number 250) and migrates upward. Most overturns lie inside the packet envelopes (yellow regions): 80% of observed overturns occur where $|\partial\hat{W}/\partial z| \geq 1.73 \times 10^{-6}$ s^{-2}, the 9-day mean value from 200 to 350 m. Regions with 6.4-m Ri $\leqslant$ 1 are also contoured in blue in each panel. Almost every overturn is encircled by either a blue or a yellow contour. Based on these observations, two types of phenomena appear to result in 2-m overturns: high 6.4-m shear layers, which are well resolved by the sonar, and internal wave groups, which are better indexed by CTD-inferred $|\partial\hat{W}/\partial z|$.

4. A statistical summary of overturning

Due to the size of the MBL dataset, it is not possible to publish depth–time maps of the entire cruise with the necessary

detail. The analyses in this section center around formation of probability density functions (PDFs) of the finescale quantities, using all observations from the 9-day, 200–350 m domain. These are then compared to corresponding PDFs computed using only observations at observed overturns (section 4a), as well as before/after them (section 4b). In section 4c an analogous procedure is applied to joint (rather than 1D) PDFs, computed between pairs of the finescale quantities.

a. Finescale statistics: Overturns

To quantify the relationship between the various finescale fields and the overturns, probability density functions (PDFs) of Richardson number, strain, and effective strain rate are estimated. Separate PDFs of the total field (259 856 Eulerian data; 339 599 s-L data) and the subset of observed overturns (10 422 Eulerian data; 5522 s-L data) are created. The overturning totals are greater than the number of observed overturning events (2227) since the events can span multiple isopycnals and depth bins.

PDFs of inverse Richardson number in the s-L frame (Fig. 15a ⊙⁼) and the Eulerian frame (Fig. 15b ⊙⁼) are in qualitative agreement with results of Pinkel and Anderson (1997a). In both reference frames, high values of Ri^{-1} are more likely when overturns are present (light black lines): 37% of overturns, compared with 30% of all observations, have $Ri^{-1}_{s-L} \geq 1$. In the Eulerian frame, 23% of overturns have $Ri^{-1}_{Eul} \geq 1$, compared with 16% of all observations.

PDFs of inverse 2-m strain for all data (Fig. 15c ⊙⁼, heavy line) are consistent with the gamma distribution of Pinkel and Anderson (1992). When only overturning data are sampled (light line), the distribution is shifted toward lower values of inverse strain: overturns are much more likely to lie in regions that are less stratified than average. This is consistent with the conclusion drawn visually from the depth–time maps (Figs. 10a ⊙⁼ and 12a ⊙⁼).

The PDF of $\log_{10}[(\partial\hat{W}/\partial z)^2]$ (Fig. 15d ⊙⁼) is indistinguishable from lognormal (dashed line, obscured by heavy line). The PDF of $(\partial\hat{W}/\partial z)^2$, considering overturning data only, is also roughly lognormal, but peaks at a higher value, demonstrating the tendency of overturns to occur where the effective strain rate magnitude is large.

The probability density of $\partial\hat{W}/\partial z$, computed using all data, is symmetric about $\partial\hat{W}/\partial z = 0$ (Fig. 16 ⊙⁼). Extreme values of $\partial\hat{W}/\partial z$ are more common than in Gaussian distributions (dashed and light lines).

b. Finescale statistics: Before and after overturns

The previous section examined differences in statistics of finescale variables under all conditions and under "unstable" conditions. That analysis is here extended to include not only overturns but periods just before and just after overturns as well. The goal is to use statistics of many overturns to construct a schematic picture of finescale conditions before and after a representative "event." Can differences be detected between "leadup" and "aftermath" of overturns? Relevant issues are the degree to which observed before/after data represent the time history of events (rather than just upstream/downstream samples of drifting features), and the amount by which the existing flow is altered by the overturning process.

Before/after PDFs of Ri^{-1} and γ^{-1} and $(\partial\hat{W}/\partial z)^2$ are presented in Figs. 17 ⊙⁼ and 18 ⊙⁼. "Leadup" PDFs of Ri^{-1} (Fig. 17a ⊙⁼), γ^{-1} (Fig. 17c ⊙⁼), and $\partial\hat{W}/\partial z$ (Fig. 18a ⊙⁼) are computed from data sampled 4 min (magenta line), 8 min (blue line), and 24 min (approximately one buoyancy period $1/N$, green line) before observed overturning events. PDFs of all data and overturning data (last section) are replotted in black and red, respectively. Figures 17b,d ⊙⁼ and Fig. 18b ⊙⁼ are the corresponding "aftermath" PDFs, computed using data sampled after overturning events. The number of observations used in forming the various PDFs (noted in the legends of fig. 17a,b ⊙⁼) differs slightly since overturns at the very beginning/end of the record cannot be used to form before/after PDFs, respectively.

Ri^{-1} and γ^{-1} PDFs (Fig. 17 ⊙⁼) each constitute a family of curves leading smoothly from "normal" to "unstable" conditions (before: Fig. 17a,c ⊙⁼), and back again (after: Fig. 17b,d ⊙⁼). Conditions one buoyancy period before overturns (magenta line) are already distinguishable from "normal" conditions (black line): the probability of higher Ri^{-1} and lower γ^{-1} values is elevated. Here γ^{-1} PDFs continue a steady progress toward "unstable" conditions. By contrast, the 4-min and 8-min before Ri^{-1} PDFs are similar to the overturning PDF. Apparently, Ri^{-1} reaches the overturning value 4–8 min before a 2-m overturn is detectable.

No asymmetry is distinguishable between "before" and "after" in the Ri^{-1} and γ^{-1} curves. Two interpretations are possible. If intrinsic time dependence is not being observed, "before" and "after" represent spatially offset "upstream" and "downstream" samples. In an isotropic ocean, no asymmetry would be seen. Alternately, the similarity between the curves

can mean that overturns affect the larger-scale flow only slightly, as in spilling surface waves. Overturns occur without drastically affecting the surrounding Ri^{-1} and γ^{-1} fields.

Effective strain rate, in contrast, exhibits differences between before (Fig. 18a ⊙) and after (Fig. 18b ⊙) periods. Relative to the curve representing normal conditions, the 24-min before curve is shifted to the right. The 4, 8-min before curves overlie the overturning curve, indicating that "overturning" conditions are present 8 min before overturns actually occur, as in the Ri^{-1} curves. After overturns, however, the behavior is different. A more rapid transition back to normal conditions is seen: the PDFs 4 min and 8 min after are shifted slightly relative to the overturning curve. That is, $|\partial\hat{W}/\partial z|$ drops immediately after overturning occurs. The difference between before and after effective strain rate PDFs suggests that perceived variability in $\partial\hat{W}/\partial z$ is due to true temporal evolution, in addition to horizontal advection. Evidently, the $\partial\hat{W}/\partial z$ field is affected by overturning. Does instability in the small-scale waves result in their destruction, leaving the larger-scale flow relatively unaffected?

c. Joint statistics

We observe correspondence between overturns and low Ri, high γ and high $|\partial\hat{W}/\partial z|$. The codependence of these quantities is thus of interest. To investigate, joint PDFs of $(\log_{10}\gamma, \partial\hat{W}/\partial z)$ and $(Ri^{-1}, \partial\hat{W}/\partial z)$ (Figs. 19 ⊙ and 20 ⊙) are formed. As in the one-dimensional study (section 4a), probability density is computed for all data over 9 days and 200–350 m, as well as for overturning observations only.

The γ and $\partial\hat{W}/\partial z$ are not independent quantities (Fig. 19a ⊙). Isopycnals that are far apart (large γ) are more likely to be converging (negative $\partial\hat{W}/\partial z$). Conversely, isopycnals closer together than average display a slight tendency to diverge. However, at extreme (large or small) values of γ, large values (positive or negative) of $\partial\hat{W}/\partial z$ are unlikely.

Considering only overturns (Fig. 19b ⊙), the PDF is shifted toward higher values of γ and exhibits more spread in $\partial\hat{W}/\partial z$ than the PDF computed from all data. These features are consistent with the one-dimensional PDFs (Fig. 15 ⊙) and the depth–time maps (Figs. 10a ⊙, 12a ⊙, and 14 ⊙). The probability density is again asymmetric in the sense that low gradient regions are associated with converging isopycnals.

The log of the ratio of the two PDFs is presented in Fig. 19c ⊙. Values greater than zero indicate higher probability density for overturning conditions than for the entire population. Regions where both the numerator and the denominator are small are left white. From 19c, overturning is much more likely for large values of γ. However, if it is to occur at smaller values of γ, then $|\partial\hat{W}/\partial z|$ must be high. It is much less likely for overturns to be associated with low γ and low $|\partial\hat{W}/\partial z|$ than for the general population.

Joint probability density functions of 6.4-m Ri^{-1} and $\partial\hat{W}/\partial z$ are presented in Fig. 20 ⊙. Simultaneous large values of general population Ri^{-1} and $\partial\hat{W}/\partial z$ are unlikely (20a). This may be due to the small implied horizontal wavelength of the $\partial\hat{W}/\partial z$ waves (appendix D), which causes their shear to be underestimated due to the separation of the sonar beams (section a in appendix A). $PDF_{overturns}$ (Fig. 20b ⊙) extends to higher values of Ri^{-1} and $|\partial\hat{W}/\partial z|$ than PDF_{all}.

The log of the ratio of the two PDFs (Fig. 20c ⊙) suggests two distinct conditions that accompany overturning: high Ri^{-1} (associated with shear instability) and high $|\partial\hat{W}/\partial z|$ (associated with the presence of wave groups). As noted, however, the $\partial\hat{W}/\partial z$ waves likely contain shear unresolved by the sonar. The probability of overturning is increased for either low Ri^{-1} and high $|\partial\hat{W}/\partial z|$ (K–H stable, waves present) or high Ri^{-1} and low $|\partial\hat{W}/\partial z|$ (K–H unstable, no waves present). A ridge connects the two regimes.

5. Dissipation rate estimates

Though no direct dissipation rate measurements are obtained during MBL, it is of value to compare several indirect estimates of mixing (appendix E). Dissipation rate parameterizations (Fig. 21 ⊙) in terms of shear [ε_{IW}, Gregg (1989), gray line] and Thorpe scales [ε_T, Thorpe (1977), Dillon (1982), black line] are evaluated.[1] In addition, an ad hoc parameterization in terms of observed $(\partial\hat{W}/\partial z)^2$ [$\varepsilon_{AP} = 500\langle(\partial\hat{W}/\partial z)^2\rangle^2$, dotted line] is computed.

The Gregg estimate involves shear squared, which is biased low by an estimated factor of $1/(0.6)$ due to the horizontal separation of the sonar beams (appendix A). Since ε_{IW} involves the fourth moment of shear, the time series has been multiplied by $1/(0.6)^2 = 2.78$ to account for this bias.

Here ε_{IW} and ε_T are similar in magnitude, usually remaining within a factor of 3 of each other. Short-term correlation between ε_{IW} and ε_T is weak, but discernible during portions of the record (e.g., rising from yearday 59.5–60, the hump from yearday 63.5–65, the increase between yearday 66–67). In general, variability is greater in ε_T than in ε_{IW}. Of course, both estimates are expected to equal true dissipation rate only in a highly averaged sense Gregg et al. (1993).

Fluctuations in the ad hoc strain rate estimate of dissipation rate, ε_{AP}, appear quite correlated with ε_T. The general features of decreasing ε over the 9-day period, as well as variation on shorter timescales (e.g., yearday 60.5–62.5, 63–64), are reproduced. The strong correspondence is not surprising given our finding that a large percentage of overturns are accompanied by high $|\partial \hat{w}/\partial z|$ (Figs. 14 ⃝ and 15d ⃝). High effective strain rates are closely tied to mixing in a depth-averaged sense as well as event-by-event.

Some correspondence is also seen between ε_{IW} and ε_{AP}. From yearday 63–68, the same general trends are seen. Apparently, depth-averaged $(\partial \hat{w}/\partial z)^2$ and 10-m shear levels (S_{10}) are related. This may be a clue to the generation mechanism of the observed small-scale waves. Do they arise from instability in larger-scale waves (indexed by S_{10}) so that S_{10} and $(\partial \hat{w}/\partial z)^2$ levels rise and fall in tandem? Perhaps the Gregg (1989) parameterization is robust because it indexes not only large-scale shear (and, indirectly, Ri), but also (more relevantly) the presence of instability-triggering waves.

Dissipation rate can also be inferred from centimeter-scale conductivity fluctuations, which were measured by a high-frequency microconductivity probe mounted below the CTD package. These are the subject of a companion paper. Here we note that dissipation rates obtained from this method are highly correlated with and similar in magnitude to ε_T. This confirms that ε_T, though approximate, is a reasonable estimate of the true mixing rate.

Cruise-mean values are summarized in Table 3 ⃝. From each dissipation rate estimate, a corresponding "dissipation Reynolds number" and effective eddy diffusivity

$$\mathrm{Re} = \frac{\overline{\varepsilon}}{\nu N^2} \qquad (9)$$

$$K_\rho = \alpha_{mix} \frac{\varepsilon}{N^2} \qquad (10)$$

can be obtained. Here, ν is the kinematic viscosity of water, and α_{mix} is the mixing efficiency, taken to be 0.2 (Oakey 1982). If we consider mean values of ε and N over 200–350 m, the deep forced region, inferred eddy diffusivities are 70%–90% of Munk's canonical value of 10^{-4} m^2 s^{-1}, significantly larger than typically observed in the open ocean (e.g., Gregg 1989). In spite of the uncertainties involved in each, the two estimates agree to within 20%.

6. Overturning: Stability and mixing

The dependence of overturn size and rate of occurrence on stratification is central to the broader issue of ocean mixing. The relationship between mean mixing rates and low-frequency (subinertial) fields must be determined before such fields can be adequately modeled. However, overturns occur in an environment characterized by the instantaneous, local buoyancy frequency, shear, and fluid acceleration. These can assume values that differ greatly from their low-frequency averages.

The dissipation accomplished by an overturning event, where vertical gradients dominate and lateral fluxes are small, is a function of the overturn size and stratification $\varepsilon_T = 0.64L_T^2 N^3$ (Dillon 1982). In the next two sections we focus on 2227 L_T, N and ε_T triplets, one for each observed overturn exhibiting $L_{max} > 2$ m.

By way of introduction, we discuss statistics of ε_T from all 2227 overturning events. Though ε_T is an inference (Dillon 1982) rather than a "ground truth" dissipation rate, its distribution is lognormal (Fig. 22 ⃝), as often observed (e.g., Gregg et al. 1993). The distribution of $\varepsilon_T = 0.64L_T^2 N^3$ differs from that of L_T (Fig. 8 ⃝) in its greater spread and lack of visbible minimum size $(L_{max} > 2)$ cutoff. For comparison with these distributions we also compute the PDF of $\varepsilon_T c \equiv \varepsilon_T \overline{N^2}/N^2$ (light line). Note that $\varepsilon_T c \sim L_T^2 N \sim K_\rho \sim$ Cox number. For higher values, the distributions of ε and $\varepsilon_T c$ are similar. At

lower values, the minimum size cutoff evident in [Fig. 8 ⊙=] is recovered in the PDF of $\mathcal{E}_T c$.

Here L_T, $\mathcal{E}$, and $\mathcal{E}_T c$ all represent different "moments" in N. Clearly, an understanding of the codependence of L_T and both local and mean stratification is called for.

a. Variability as a function of instantaneous stratification

We first investigate statistical relationships between L_T, $\mathcal{E}_T$ and the instantaneous bouyancy frequency $N(t, z)$. Considering only the overturns, L_T and $\mathcal{E}_T$ from discrete events are averaged with corresponding values from other events at like N. Forty averaging bins, evenly spaced in $\log_{10}N$, are established between 0.1 and 10 cph.

Over instantaneous bouyancy frequency ranges, $0.8 \lesssim N \lesssim 3$ cph, $L_T \sim N^{-1/2}$ ([Fig. 23a ⊙=]) and $\mathcal{E}_T \sim N^2$ ([Fig. 23b ⊙=]). There are very few realizations at the more extreme values of N. (The mean buoyancy frequency does not fall below 2 cph in this domain, [Fig. 3 ⊙=].) Sampling error reduces the precision of the relationship at these extreme N. We emphasize that decreasing local N does not imply increasing depth since strains at the MBL site are sufficient that all values of N are deformed into a wide range in N. We also note that a fixed rms error in density, $\Delta\rho = 3 \times 10^{-4}$ kg m^{-3} (appendix B), establishes apparent overturns of magnitude

$$L_{T,noise} = \Delta\rho \Big/ \frac{\partial\rho}{\partial z} = \frac{g\Delta\rho}{\rho}N^{-2}. \qquad (11)$$

This function ([Fig. 23 ⊙=], dash–dot line) is much steeper than, and well below, the observed relation, indicating that that instrument noise does not dominate these overturn estimates.

b. Variability as a function of mean stratification

Typically, the N dependence of $\mathcal{E}$ is investigated in terms of long-term Eulerian averages, where average dissipation rate estimates are compared with mean stratification, $\overline{N}$. The MBL observations are here viewed in this format. To convert from averages over "event" to averages over time, the overturning fraction $p_o(z)$ is introduced. To compute p_o, an overturn index matrix is formed, with bins every meter in depth, every 4 min in time, over the 9-day data record. The matrix is initially zero filled.

Iterating through each of the 2227 overturns, a value of unity is stored in all bins spanned by that overturn. Averaging in time then produces the fraction $p_o(z)$ of the water column sampled (at depth z), which is occupied by overturns. (The depth mean of p_o from 200 to 350 m yields the overall overturning fraction, 3.06%.)

The overturning fraction p_o is then plotted versus the 9-day mean $\overline{N}$ ([Fig. 24 ⊙=]). Unfortunately, $\overline{N}$ exhibits only a small range of variation (2–3 cph) over the 200–350 m observation window. To widen the range of $\overline{N}$ to 4 cph the study is extended upward, including overturns to depths of 120 m (thin line). For $\overline{N} \geq 2.5$ cph $p_o(\overline{N}) \sim \overline{N}^{-3}, \overline{N}^{-2}$ (dashed lines). At lower $\overline{N}$, p_o appears constant.

A similar procedure can be used to compute the Eulerian average dissipation, $\mathcal{E}_{mean}(z)$. Instead of storing unity in the overturn index matrix, $\mathcal{E}_T = 0.64L_T^2 N^3$ is stored for each overturn. Averaging across time produces $\mathcal{E}_{mean}(z)$, which is plotted versus $\overline{N}(z)$ in [Fig. 25a ⊙=].

For $\overline{N} \geq 2.5$ cph, $\mathcal{E}_{mean} \sim \overline{N}^2$, consistent with previous observations $\mathcal{E}_{mean} \sim \overline{N}^1 - \overline{N}^2$ ([Gargett and Osborn 1981]; [Gargett and Holloway 1984]; [Lueck et al. 1983]; [Gregg et al. 1986]) and with theoretical predictions $\mathcal{E}_{mean} \sim \overline{N}^2$ in terms of wave–wave interactions ([Henyey et al. 1986]; [McComas and Müller 1981]; [Gregg 1989]; [Polzin et al. 1995]). At greater depths, $\overline{N} \lesssim 2.5$ cph, a different regime is encountered. Dissipation increases with increasing depth, decreasing $\overline{N}$. In this depth range, rms shear also begins to increase with depth ([Fig. 5 ⊙=]), suggesting the influence of seafloor/coastal wave generation. The [Gregg (1989)] dissipation parameterization [Eq. (E1)] explicitly accounts for both shear and stratification ([Fig. 25 ⊙=], light line). For the regime $\overline{N} \geq 2.5$ cph, the two dissipation rate estimates show $\mathcal{E} \sim \overline{N}^2$. For $\overline{N} \lesssim 2.5$ cph,

both show the increase in dissipation with depth. Though agreement in this range is not perfect (the Gregg parameterization exhibits steeper slope), the similarity in general form of the two estimates (one involving only CTD observations and the other involving primarily sonar data) is significant.

Under both parameterizations, strong diapycnal diffusivities are implied by these results (Fig. 25b ⊙). Estimates of K_ρ increase with depth for $\overline{N} \lesssim 3$ cph, exceeding 10^{-4} m^2 s^{-1} at the bottom of the record, still 1000 m above the seafloor. Polzin et al. (1997) observed heightened K_ρ values (up to 10^{-3} m^2 s^{-1}) above the mid-Atlantic Ridge, decreasing upward into the water column. Upward-propagating breaking waves generated by flow over the ridge topography are assumed to be responsible. Given the proximity of the MBL site to topography and the observed $\partial \hat{w}/\partial z$ waves that appear to be breaking, the similarity in magnitude and depth dependence of MBL-inferred K_ρ values and those of Polzin et al. (1997) is interesting. Are the same processes at work in both locations?

7. Mixing, overturn size, and background strain

We have seen that mixing occurs preferentially in regions of lower than average N^2. To what extent do finescale dynamics conspire to minimize the buoyancy flux, which depends on N^2? To address this issue we can compute the conditional sums:

$$c_{\gamma^{-1}}(x) \equiv \sum_{i | \gamma^{-1} < x} \varepsilon_{T_i} L_{P_i}. \qquad (12)$$

Here ε_T and L_T represent the Thorpe inferred dissipation and patch size in depth and time of the ith event. The sum represents the total dissipation over those events associated with inverse strain $\gamma^{-1} < x$. The normalized equivalent

$$C_{\gamma^{-1}}(x) \equiv \frac{c_{\gamma^{-1}}(x)}{c_{\gamma^{-1}}(\infty)} = \frac{c_{\gamma^{-1}}(x)}{\overline{\varepsilon_T}} \qquad (13)$$

gives the fraction of ε_T associated with events occurring with inverse strain $\gamma^{-1} < x$. An estimate of $C_{\gamma}-1(x)$ is presented in Fig. 26a ⊙, where data are binned in 40 intervals over $0 < \gamma^{-1} < 2$. Overturns occurring where $\gamma^{-1} < 1$ (weaker than average stratification) are associated with 95% of the Thorpe-inferred dissipation rate. Evidently, the strong tendency for overturns to occur in regions of lower than average N overcomes the N^3 weighting in the individual event dissipations.

Is most mixing accomplished by large, rare overturns or smaller, more frequent ones? The contribution to mixing of each size class can again be quantified in terms of a conditional sum:

$$C_{L_T}(x) \equiv \sum_{i | L_T < x} \varepsilon_{T_i} L_{P_i} / \overline{\varepsilon_T}, \qquad (14)$$

which gives the fractional contribution to overall dissipation from events with rms Thorpe scale less than x. Our minimum overturn size restriction, $L_{max} < 2$ m is manifest by the lack of contributions from $L_T < 1$ m. Extrapolation to $L_T = 0$ suggests that inclusion of smaller overturns would affect ε only little (<10% or so). The slope of $C(x)$ is approximately constant for $L_T \lesssim 8$ m, indicating that overturns in each size class contribute comparably to total dissipation. Approximately half of dissipation is accomplished by those overturns with $L_T \lesssim 5$ m, 80% with $L_T \lesssim 8$ m. Larger overturns contribute rather less: only 10% results from the largest overturns, $L_T > 10$ m. It appears that, due to their increased frequency of occurrence, more modest overturns outweigh the "big bangs" in dissipating kinetic energy. On the other hand, 5–7 m overturns are still quite influential by open ocean standards.

In a simple statistical mixing model based on K–H instability, Pinkel and Anderson (1997b) suggest that 3-m overturns are the dominant contributors to ocean mixing at the Garrett–Munk energy (shear variance) level. Interestingly, as energy levels advance above GM, the (modeled) contribution from larger overturns increases rapidly. These model results are generally consistent with the MBL observations.

8. Summary

MBL is an energetic coastal site. Strong frontal activity and offshore jets characterize the region. Baroclinic tidal activity is

confined in both depth and time, exhibiting a pronounced raylike character. In contrast with the open ocean, $\overline{S}^2$ increases with depth below 250 m. We take this as an indication of midwater or bottom forcing of the finescale fields. Large eddy diffusivities ($K_\rho = 0.70$–0.89×10^{-4} m^2 s^{-1}) are implied by parameterizations of Gregg (1989) and Dillon (1982).

Density overturns are identified as inversions of 2-m vertical extent or greater that are detected simultaneously in density, temperature, and conductivity profiles. Overturning is most likely to occur in regions of high strain (lower-than-average stratification) and low 6.4-m Ri. Strongest correspondence, however, is seen between overturning and occurrences of high effective strain rate magnitude. Intense strain rates appear to be associated with groups of small-scale internal waves. Also seen are regions in which the 6.4-m Ri remains critical for hours, with no overturning observed. Although overturns smaller than 2 m might be present, the long-term stability of these regions is surprising.

Probability density functions of γ^{-1}, Ri^{-1}, and $(\partial \hat{W}/\partial z)^2$ are computed for all data, as well as for data sampled at, before, and after observed 2-m overturns. Typically, γ^{-1} and Ri begin to differ from background conditions approximately one buoyancy period before overturning. Here γ^{-1} steadily decreases to its minimum value at the overturn, then gradually returns, approaching normal values after another buoyancy period. The Ri drops to its minimum value 4–8 min before the overturn, remaining there until 4–8 min afterward. It then gradually returns to normal. For γ^{-1} and Ri^{-1}, "leadup" and "aftermath" are indistinguishable.

By contrast, $(\partial \hat{W}/\partial z)^2$ increases to a maximum value 4–8 min before the overturn, but drops quickly afterward, before continuing its return to normal values. One possible interpretation is that overturning results when small-scale internal waves, propagating through a slowly varying background flow, become unstable. The larger-scale flow (indexed by γ^{-1}, Ri^{-1}) is relatively unaffected by overturning, while the waves themselves [indexed by $(\partial \hat{W}/\partial z)^2$] are altered significantly.

Estimates of depth-mean dissipation rate employing overturning scales (Thorpe 1977; Dillon 1982), and 10-m shear (Gregg 1989) are correlated in time. Short-term (~ 1 day) differences are seen since each method requires extensive averaging in order to be accurate. However, long-term mean values agree to within 20%, and both quantities exhibit the same scaling with mean stratification ($\varepsilon_{\text{mean}} \sim \overline{N}^2$ for $\overline{N} \geq 3$ cph, $\varepsilon_{\text{mean}}$ increasing with decreasing $\overline{N}$ at greater depths).

9. Conclusions

The goal of this study has been to document the finescale conditions that accompany overturning. While 6.4-m Ri is a factor in determining overturn locations, the presence of small-scale waves associated with high $|\partial \hat{W}/\partial z|$ appears to be even more important. The Gregg (1989) dissipation rate parameterization (which involves only finescale shear S_{10}) is consistent in level and $\overline{N}$-dependence with overturn-inferred dissipation rate (Fig. 25a ⊙). That is, in the long-term average, the local, finescale shear determines the local dissipation rate. Apparently, the history that the small-scale "test waves" bring into a region is unimportant. Indeed, the vertical propagation of the waves is clearly inhibited, as seen from Figs. 13 ⊙ and 14 ⊙. Presumably, they interact strongly with the local finescale environment. The observed waves appear to be an important link in the energy transfer from large scales to turbulence.

The observed waves must contain shear at scales unresolved by the sonar. Indeed, the waves are clearly evident in s-L records of "slant shear" obtained from individual sonar beams (which suffer from limited vertical, but not horizontal, resolution). In spite of the measurement challenge presented by the waves, these records show correspondence with the CTD-based observations. A detailed CTD/sonar study of the waves is the subject of a future paper. For the present discussion, we have considered a canonical wave with observed $|\partial \hat{W}/\partial z| = 1 \times 10^{-3}$ s^{-1}, $m = 0.08$ cpm, and $k = 5.7 \times 10^{-3}$ cpm (appendix D). From linear theory, such a wave has a peak shear of order 1.4×10^{-2} s^{-1}. In a region where $N = 3$ cph (i.e., neglecting the wave's strain), this shear corresponds to Ri = 0.14. While the assumption of linearity is dubious and the influence of horizontal advection is significant, the waves are clearly capable of producing Ri low enough for K–H instability.

It is tempting to associate the "high $|\partial \hat{W}/\partial z|$, high Ri" overturns of Fig. 20 ⊙ with convective instability and the "low $|\partial \hat{W}/\partial z|$, low Ri" overturns with K–H instability. However, the intrinsic shears of the small-scale breaking waves are poorly resolved by our sonar. We thus cannot claim a definitve determination of the breaking mechanism.

Regardless, the association of overturning events with the presence of small-scale internal wave groups (which, in turn, are closely tied to larger-scale shear) represents a step forward in our understanding of ocean mixing. An improved description of the dynamics, as well as the climatology, of these waves is called for.

REFERENCES

Anderson, S. P., 1993: Shear, strain and thermohaline vertical fine structure in the upper ocean. Ph.D. thesis, University of California, San Diego. [Available from Scripps Institution of Oceanography, 9500 Gilman Drive, La Jolla, CA 92093-0208.].

Broutman, D., and W. R. Young, 1986: On the interaction of small-scale oceanic internal waves with near-inertial waves. *J. Fluid Mech.,* **166,** 341–358..

Dillon, T. M., 1982: Vertical overturns: A comparison of Thorpe and Ozmidov length scales. *J. Geophys. Res.,* **87,** 9601–9613..

Galbraith, P. S., and D. E. Kelley, 1996: Identifying overturns in CTD profiles. *J. Atmos. Oceanic Technol.,* **13,** 688–702..

Gargett, A. E., and T. Osborn, 1981: Small-scale shear measurements during the Fine and Microstructure Experiment (FAME). *J. Geophys. Res.,* **86** (C3), 1929–1944..

—— ,and G. Holloway, 1984: Dissipation and diffusion by internal wave breaking. *J. Mar. Res.,* **42,** 15–27..

—— ,P. J. Hendricks, T. B. Sanford, T. R. Osborn, and A. J. Williams III, 1981: A composite spectrum of vertical shear in the upper ocean. *J. Phys. Oceanogr.,* **11,** 1258–1271.. Find this article online

Garrett, C., and W. Munk, 1972: Space–time scales of internal waves. *Geophys. Fluid Dyn.,* **2,** 225–264..

—— ,and —— ,1975: Space–time scales of internal waves: A progress report. *J. Geophys. Res.,* **80,** 291–297..

Gregg, M. C., 1989: Scaling turbulent dissipation in the thermocline. *J. Geophys. Res.,* **94** (C7), 9686–9698..

—— ,E. A. D'Asaro, T. J. Shay, and N. Larson, 1986: Observations of persistent mixing and near-inertial waves. *J. Phys. Oceanogr.,* **16,** 856–885.. Find this article online

—— ,H. E. Seim, and D. Percival, 1993: Statistics of shear and turbulent dissipation profiles in random internal wave fields. *J. Phys. Oceanogr.,* **23,** 1777–1799.. Find this article online

Hazel, P., 1972: Numerical studies of the theory of inviscid stratified shear flows. *J. Fluid Mech.,* **51,** 39–61..

Hebert, D., J. N. Moum, C. A. Paulson, and D. R. Caldwell, 1992: Turbulence and internal waves at the equator. Part II: Details of a single event. *J. Phys. Oceanogr.,* **22,** 1346–1356.. Find this article online

Henyey, F. S., J. Wright, and S. M. Flatté, 1986: Energy and action flow through the internal wave field. *J. Geophys. Res.,* **91,** 8487–8495..

Howard, L. N., 1961: Note on a paper of John W. Miles. *J. Fluid Mech.,* **10,** 509–512..

Kunze, E., M. G. Briscoe, and A. J. Williams III, 1990: Observations of shear and vertical stability from a neutrally buoyant float. *J. Geophys. Res.,* **95** (C10), 18 127–18 142..

Lueck, R. G., and J. J. Picklo, 1990: Thermal inertia of conductivity cells: Observations with a Sea-Bird cell. *J. Atmos. Oceanic Technol.,* **7,** 756–768..

—— ,W. R. Crawford, and T. R. Osborn, 1983: Turbulent dissipation over the continental slope off Vancouver Island. *J. Phys. Oceanogr.,* **13,** 1809–1818.. Find this article online

Marmorino, G. O., L. J. Rosenblum, and C. L. Trump, 1987: Fine-scale temperature variability: The influence of near-inertial waves. *J. Geophys. Res.,* **92,** 13 049–13 062..

McComas, C. H., and P. Müller, 1981: Time scales of resonant interaction among oceanic internal waves. *J. Phys. Oceanogr.,* **11,** 139–147.. Find this article online

Miles, J. W., 1961: On the stability of heterogeneous shear flows. *J. Fluid Mech.,* **10** (4), 496–508..

Morison, J., R. Anderson, N. Larson, E. D'Asaro, and T. Boyd, 1994:The correction for thermal-lag effects in Sea-Bird CTD data. *J. Atmos. Oceanic Technol.,* **11,** 1151–1164..

Moum, J. N., D. Hebert, C. A. Paulson, and D. R. Caldwell, 1992: Turbulence and internal waves at the equator. Part I: Statistics from towed thermistors and a microstructure profiler. *J. Phys. Oceanogr.,* **22,** 1330–1345.. Find this article online

Oakey, N. S., 1982: Determination of the rate of dissipation of turbulent energy from simultaneous temperature and velocity shear microstructure measurements. *J. Phys. Oceanogr.,* **12,** 256–271.. Find this article online

Orlanski, I., and K. Bryan, 1969: Formation of thermocline step structure by large-amplitude internal waves. *J. Geophys. Res.,* **74,** 6975–6983..

Peters, H., M. C. Gregg, and T. B. Sanford, 1995: On the parameterization of equatorial turbulence: Effect of fine-scale variations below the range of the diurnal cycle. *J. Geophys. Res.,* **100** (C9), 18 333–18 348..

Pinkel, R., and S. Anderson, 1992: Toward a statistical description of finescale strain in the thermocline. *J. Phys. Oceanogr.,* **22,** 773–795.. Find this article online

—— ,and J. A. Smith, 1992: Repeat sequence coding for improved precision of Doppler sonar and sodar. *J. Atmos. Oceanic Technol.,* **9,** 149–163..

—— ,and S. Anderson, 1997a: Shear, strain and Richardson number variations in the thermocline. Part I: Statistical description. *J. Phys. Oceanogr.,* **27,** 264–281.. Find this article online

—— ,and —— ,1997b: Shear, strain and Richardson number variations in the thermocline. Part II: Modeling mixing. *J. Phys. Oceanogr.,* **27,** 282–290.. Find this article online

—— ,J. Sherman, J. Smith, and S. Anderson, 1991: Strain: Observations of the vertical gradient of isopycnal vertical displacement. *J. Phys. Oceanogr.,* **21,** 527–540.. Find this article online

Polzin, K. L., J. M. Toole, and R. W. Schmitt, 1995: Finescale parameterizations of turbulent dissipation. *J. Phys. Oceanogr.,* **25,** 306–328.. Find this article online

—— ,—— ,J. R. Ledwell, and R. W. Schmitt, 1997: Spatial variability of turbulent mixing in the abyssal ocean. *Science,* **276,** 93–96..

Sandwell, D. T., and W. H. F. Smith, 1997: Marine gravity anomaly from Geosat and ERS-1 altimetry. *J. Geophys. Res.,* **102** (B5), 10 039–10 054..

Seim, H. E., and M. C. Gregg, 1994: Detailed observations of a naturally occuring shear instability. *J. Geophys. Res.,* **99** (C5), 10 049–10 073..

Sherman, J. T., 1989: Observations of fine scale vertical shear and strain in the upper ocean. Ph.D. thesis, University of California, San Diego..

Smith, J., 1998: Evolution of Langmuir circulation during a storm. *J. Geophys. Res.,* **103** (C6), 12 649–12 668..

Sun, H., and E. Kunze, 1999: Internal wave–wave interactions. Part I: The role of internal wave vertical divergence. *J. Phys. Oceanogr.,* **29,** 2886–2904.. Find this article online

Thorpe, S., 1977: Turbulence and mixing in a Scottish loch. *Philos. Trans. Roy. Soc. London, Ser. A,* **286,** 125–181..

Wijesekera, H. W., T. M. Dillon, and L. Padman, 1993: Some statistical and dynamical properties of turbulence in the ocean pycnocline. *J. Geophys. Res.,* **98,** 22 665–22 679..

APPENDIX A

10. Velocity and Shear Measurement Errors

Horizontal beam separation and sonar noise affect shear estimates. The former biases 6.4-m squared shear S^2 low, while the latter biases S^2 high. An understanding of these effects is of use in interpreting the observations. Here, "worst case" estimates of the magnitude of the biases are presented.

a. Finite beam separation

Estimates from back-to-back beams are combined to obtain horizontal velocity. For the present study where beams are directed $\theta = 30°$ from the vertical (Fig. 1 ⊙▬), the horizontal beam separation Δx increases from 20 m at the top of our records (100-m depth), to 360 m at the bottom (400-m depth). Each beam registers the component of velocity parallel to the beam, where positive velocity indicates motion toward the sonar. Consider the *FLIP* sonar located at $(x = 0, y = 0, z = -87$ m), oriented such that back-to-back beams 1 and 3 are aligned with zonal flow. Then, in terms of "oceanic" velocity components u and w, the beam "slant" velocities b_1 and b_3 are given by

$$b_1(z) = u\left(-\frac{\Delta x}{2}, z\right) \sin\theta + w\left(-\frac{\Delta x}{2}, z\right) \cos\theta \quad (A1)$$

$$b_3(z) = -u\left(\frac{\Delta x}{2}, z\right) \sin\theta + w\left(\frac{\Delta x}{2}, z\right) \cos\theta. \quad (A2)$$

Neglecting horizontal variations in w, the Janus horizontal velocity estimate is given by

$$\overline{u}(0, 0, z) \equiv \frac{1}{2}\left[u\left(-\frac{\Delta x}{2}, z\right) + u\left(\frac{\Delta x}{2}, z\right)\right]$$

$$= \frac{b_1(z) - b_3(z)}{2 \sin\theta}. \quad (A3)$$

Shears are then obtained by differencing in depth.

Motions of horizontal scale comparable to the beam separation or smaller are not properly represented in a Janus description. Specifically, $u(x, 0, z)$ can be represented as the Fourier transform of its horizontal wavenumber components:

$$u(x, 0, z) = \frac{1}{\sqrt{2\pi}} \int \tilde{u}(k, z) \, e^{ikx} dk. \quad (A4)$$

By substituting (A4) into (A3) it is easily shown that the transfer function that relates spectra of true "oceanic" velocity u (x) and Janus velocity is

$$T(k) = \cos^2(\pi k \Delta x), \quad (A5)$$

where k is in cyclic units. The $T(k)$ for shear is the same as that for velocity. Here $T(k)$ has a zero at $k = \Delta x/2$: waves of wavelength $2\Delta x$ are not registered at all in Janus estimates since signals at the two beams are 180° out of phase. In contrast, all of the variance of a wave of length Δx is registered (although it is aliased). We can define an underresolution factor,

$$r \equiv \frac{\int S(k)T(k) \, dk}{\int S(k) \, dk}, \quad (A6)$$

which represents the fraction of variance resolved by the sonar for a given input shear spectrum $S(k)$, where $r = 1$ represents full resolution.

While a direct estimate of $S(k)$ is not available, it is possible to form a precise lower bound for r directly from our data. We compare the Janus shear estimates with counterparts formed from individual beams, which are not subject to beam-separation distortion. We define

$$\hat{r}(z, t) = \frac{\left\langle \left(\frac{\partial \overline{u}}{\partial z}\right)^2 \right\rangle}{\max\left(\left\langle \left(\frac{\partial u_1}{\partial z}\right)^2 \right\rangle, \left\langle \left(\frac{\partial u_3}{\partial z}\right)^2 \right\rangle \right)}. \qquad (A7)$$

Here u_1 and u_3 are the slant velocities at each beam, normalized as if they were purely horizontal velocities; that is, $u_1 = b_1/\sin\theta$, $u_3 = b_3/\sin\theta$. Given that (A7) selects the maximum of the individual beam values, $\hat{r} \leq 1$. The angle brackets denote averaging over a specific depth–time interval. The individual beam shears do not suffer the effects of spatial aliasing. However, they include the vertical strain rate along with horizontal motions (see below). Thus, $\hat{r}$ is a worst case metric of spatial aliasing.

Here $\hat{r}(z, t)$ is computed for back-to-back beam pairs 1, 3 (Fig. A1a ⊙━) and 2, 4 (Fig. A1b ⊙━) for yeardays 67.5–68; $\hat{r}$ varies between about 0.4 and 1. Values near 1 presumably represent the local dominance of larger-horizontal-wavelength features. Using $\hat{r}(z, t)$, a lower bound on 6.4-m Ri may be determined for any desired depth–time region. For example, yearday 67.75, 150 m (Fig. 10c ⊙━) shows overturning in a region where Ri ≥ 2. In this region, $\hat{r} \geq 0.6$; therefore, it is possible to say with confidence that 6.4-m Ri ≥ 1.2. From the probability density function of $\hat{r}$ (Fig. A2 ⊙━, heavy lines), it is seen that $\hat{r} \leq 0.5$ less than 4% of the time. From this pessimistic analysis, we conclude that 6.4-m S^2 and Ri^{-1} estimates are rarely biased as low as a factor of 2, but are frequently about 60% of their true values.

Is $\hat{r}$ an overly pessimistic estimate? After all, the "beam shear"

$$\frac{\partial u_1}{\partial z} = \frac{\partial u}{\partial z} + \frac{\partial u}{\partial x}\tan\theta + \frac{\partial w}{\partial x} + \frac{\partial w}{\partial z}\cot\theta \qquad (A8)$$

has a variance clearly greater than the true vertical shear. The effect of the $\partial \hat{w}/\partial z$ term on $\hat{r}$ can be estimated by subtracting different values of $\overline{(\partial w/\partial z)^2}$ from the denominator of (A7).

$$\hat{r}'(z, t) = \frac{\left\langle \left(\frac{\partial \overline{u}}{\partial z}\right)^2 \right\rangle}{\max\left(\left\langle \left(\frac{\partial u_1}{\partial z}\right)^2 \right\rangle, \left\langle \left(\frac{\partial u_3}{\partial z}\right)^2 \right\rangle \right) - \cot^2\theta \overline{\left(\frac{\partial w}{\partial z}\right)^2}}.$$

$$(A9)$$

PDFs of $\hat{r}'$ are plotted on the same axes as PDFs of $\hat{r}$ (Fig. A2 ⊙━). For simplicity, the mean value $\overline{(\partial \hat{w}/\partial z)^2}$, as determined from CTD observations, is used as a reference. Values of $\overline{(\partial \hat{w}/\partial z)^2}$ used are 25 (light dashed line), 50 (light dash–dot line), and 100 (light solid line) percent of the 9-day mean value of $\overline{(\partial \hat{w}/\partial z)^2}_{cruise} = 1.73 \times 10^{-6}$ s^{-2}. As the modeled strain rate variance is increased, the PDFs of $\hat{r}$ move toward higher values. Eventually, some values ≥ 1 are obtained, indicating that the assumed $\overline{(\partial \hat{w}/\partial z)^2}$ value is too high for some observations. Note that though $\partial \hat{w}/\partial z$ includes effects of advection [Eq. (8)], relatively low values produce substantial shifts. Recalling, too, that contributions to (A9) from $\partial w/\partial x$ and $\partial u/\partial x$ have not been considered, we conclude that $\hat{r}$ is indeed a pessimistic metric.

b. Velocity imprecision

Here S^2 estimates are biased high by imprecision in the sonar-derived estimates of horizontal velocity. For example, if measured shear

where d_1 and d_2 are noise (assumed uncorrelated) in each velocity estimate, then estimated squared shear S^2_s is elevated relative to the true oceanic squared shear:

$$S^2_s = \left(\frac{\Delta u}{\Delta z}\right)^2 + 2\frac{d^2}{(\Delta z)^2}, \qquad \text{(A11)}$$

where $d^2 = \langle d^2_1 \rangle = \langle d^2_2 \rangle$. As one pushes for higher vertical resolution, the expected velocity difference across Δz decreases, while the measurement imprecision d grows (due to shorter transmitted pulses). The present look at finescale shear is only possible with the development of coded pulses, which minimize d for given pulse length. An upper bound on the noise is given by comparing estimates of vertical velocity between the two back-to-back beam pairs. In a noise-free environment with no spatial variability, the two estimates of w, given by

$$w_{13} = \frac{(b_1 + b_3)}{2 \cos\theta}, \qquad \text{(A12)}$$

$$w_{24} = \frac{(b_2 + b_4)}{2 \cos\theta}, \qquad \text{(A13)}$$

should be identical. The noise is

$$n = \frac{(w_{24} - w_{13})}{2 \tan^2\theta},$$

where the factor $1/\tan^2\theta$ converts n from a vertical to an equivalent horizontal velocity noise. Note that n represents a conservative upper bound on the noise, as horizontal variability between the beams are included. A signal to noise ratio R_{SN} may be computed as a function of vertical wavenumber m and frequency ω from the noise spectrum $S_n(\omega, m)$ [the Fourier transform in space and time of $n(z, t)$] and the spectrum $S_{\bar{u}}(\omega, m)$ of $\bar{u}$:

$$R_{SN}(\omega, m) = \frac{S_{\bar{u}}(\omega, m) - S_n(\omega, m)}{S_n(\omega, m)}. \qquad \text{(A14)}$$

We present an estimate of R_{SN}, computed from 100 to 400 m, over yearday 67.5–68 (Fig. A3 ⊙). At low wavenumbers and frequencies, R_{SN} exceeds 10, falling as frequency and wavenumber increase. As the vertical scale of interest decreases, the required averaging time increases. Given our finding that overturns often occur where Ri is higher than expected, rather than lower, we have erred on the side of including some noise, rather than averaging out real fluctuations at these timescales.

APPENDIX B

11. Strain and Effective Strain Rate Measurement Errors

Random fluctuations in density estimates introduce uncertainty in isopycnal depth determinations. To what extent does noise influence γ and $\partial\hat{w}/\partial z$?

Uncertainty in isopycnal displacement η is given by

$$\Delta\eta = \frac{g\Delta\rho}{\rho N^2}, \qquad \text{(B1)}$$

where $g = 9.8$ m s^{-2}, $\rho = 1026$ kg m^{-3}, and $\Delta\rho$ is the rms density noise. Sherman (1989) estimates $\Delta\rho = 3 \times 10^{-4}$ kg m^{-3} for the PATCHEX experiment, which used the same CTD and matching procedure as in MBL. Here $\Delta\rho$ estimated for the MBL data (from the magnitude of density fluctuations unaccompanied by temperature signatures) is 2×10^{-4} kg m^{-3}. Sherman's value is retained as a conservative estimate. Equation (B1) yields $\Delta\eta = 15$ cm for the MBL cruise mean value, $N = 2.53$ cph. From 5, γ involves a depth difference of two isopycnal displacement estimates η. If each contains rms noise $\Delta\eta$, then mean square noise in strain is given by

$$\gamma^2_{\text{noise}} = \frac{2(\Delta\eta)^2}{(\Delta z)^2}. \qquad \text{(B2)}$$

Combining (B1) and (B2) and the relation $\gamma = \overline{N^2}/N^2$ yields the fractional uncertainty in γ estimates

$$\frac{\Delta\gamma}{\gamma} = \frac{\sqrt{2}}{\Delta z} \frac{g\Delta\rho}{\rho\overline{N}^2}. \qquad \text{(B3)}$$

Substituting $\Delta z = 2$ m and the values used above yields $\Delta\gamma/\gamma = 0.1$, indicating that individual strain estimates are precise to within 10%. Here $\partial\hat{w}/\partial z$ involves differencing in time and in space:

$$\frac{\partial\hat{w}}{\partial z} \approx \frac{1}{\Delta t}\frac{1}{\Delta z}\{[\eta(t + \Delta t, z + \Delta z) - \eta(t + \Delta t, z)]$$
$$- [\eta(t, z + \Delta z) - \eta(t, z)]\}. \qquad \text{(B4)}$$

If each of the four separate isopycnal depth estimates in (B4) contains rms noise $\Delta\eta$, uncertainty in $(\partial\hat{w}/\partial z)^2$ is given by

$$\left(\frac{\partial\hat{w}}{\partial z}\right)^2_{\text{noise}} = \frac{4(\Delta\eta)^2}{(\Delta z)^2(\Delta t)^2}. \qquad \text{(B5)}$$

Substituting $\Delta z = 2$ m, $\Delta t = 240$ s, $\Delta\eta = 0.15$ m yields $(\partial\hat{w}/\partial z)^2_{\text{noise}} = 3.9 \times 10^{-7}$ s^{-2} in individual estimates. Averaging each over two time bins and two depth bins reduces noise variance by 4 and results in $(\partial\hat{w}/\partial z)^2_{\text{noise}} = 1.0 \times 10^{-7}$ s^{-2}, rms ($\partial\hat{w}/\partial z)_{\text{noise}} = 3.2 \times 10^{-4}$ s^{-1}. Visual determination of the green noise "floor" level in Fig. 14 ⊙ (by eye, $1\text{–}2 \times 10^{-7}$ s^{-2}) supports this estimate. We conclude from this analysis that the visible sloping features of the $\partial\hat{w}/\partial z$ field in Fig. 13 ⊙ [magnitude $1\text{–}2$ ($\times 10^{-3}$ s^{-1})] are 3–6 times the rms noise level.

APPENDIX C

12. Lateral Intrusions

Lateral intrusions can displace isopycnal surfaces, thereby introducing strainlike features. Intrusive activity is anticipated at the MBL site. Can it be distinguished from internal wave straining? To detect intrusions, we form time–depth series of temperature variation at fixed density ρ (Fig. C1a ⊙). Here, the temperature anomaly along each isopycnal surface, defined relative to the time-averaged temperature along the isopycnal, is presented.

Much advective activity is seen. One distinct water mass is replaced by another, warmer, one at around yearday 67.7. Some vertical "interleaving" is seen at the interface between the two water masses and elsewhere. Both the time and depth scales of this intrusive activity contrast with those of the strain field of Fig. 12a ⊙.

To emphasize the finescale intrusive variability, the derivative $\partial T/\partial\rho$ is formed, and again plotted in a s-L reference frame (Fig. C1b ⊙). The dominant signal is seen in the upper portion of the record, in contrast to the strain record (Fig. 12a ⊙). Linear internal waves are incapable of altering temperature along isopycnals, except by horizontally displacing water of

different characteristics. The strain field is affected by the advection of lateral features shown in Fig. C1 ⃝, and by internal waves as well. Comparison of Fig. C1 ⃝ and Fig. 12a ⃝ shows that though both fields are active and complex, there is little correspondence. We conclude that the variability in the strain field is not primarily due to lateral intrusions.

APPENDIX D

13. Estimating Intrinsic Frequency

Are the high-frequency waves seen in MBL really high frequency? Advection by larger waves and background currents can cause a wave's observed frequency ω_{obs} to differ from its intrinsic frequency ω_{int}. The frequency shift depends on horizontal wavenumber k, the magnitude of the advective velocity $\mathbf{U}$, and the angle between current and wave propagation directions θ:

$$\omega_{int} = \omega_{obs} - |k||U| \cos\theta. \text{(D1)}$$

Intrinsic frequency and horizontal wavenumber may be estimated using the dispersion relation for linear internal waves

$$\omega_{int} = \sqrt{\frac{N^2k^2 + f^2m^2}{k^2 + m^2}}. \qquad \text{(D2)}$$

Here f is the Coriolis frequency, N the buoyancy frequency, and m the vertical wavenumber; θ is the angle between current and wave propagation directions, and N, f, m, and ω_{obs} are observed quantities. Consider a representative, well-defined wave packet (Fig. 13b ⃝, 300 m and yearday 67.72), with $m = 0.08$ cpm, $\omega_{obs} = 4$ cph. Typical values of $|U|$ are 20 cm s^{-1}. Using $N = 2$ cph, $f \approx 1/24$ cph, and these values of m, ω_{obs}, and $|U|$, curves D1 and D2 are plotted on the same axes, for different values of θ(Fig. D1 ⃝). All frequencies and wavenumbers are expressed in cyclic units. The intersections of the colored curves with the gray one yield values of ω_{int} and k, consistent with linear theory for the indicated value of θ. Some Doppler shifting must have occurred, for the observed frequency $\omega_{obs} = 4$ cph is higher than local $N = 2$ cph. The minimum value of ω_{int} (assuming maximum Doppler shifting) is 0.14 cph (7-h period). A lower bound on k is 5.7×10^{-3} cpm (180-m wavelength), implying a horizontal phase velocity $c_p = \omega/k = 0.7$ cm s^{-1}. If angles of incidence were uniformly distributed, half of all values would lie between the 0° and 45° curves (less than a factor of 2 difference). Higher assumed values of θ result in lower estimates of ω_{int}. Assuming $|U| = 30$ cm s^{-1}, for example, places maximally Doppler shifted waves of the dimensions above at near-tidal frequencies, with horizontal wavelength around 270 m.

APPENDIX E

14. Dissipation Rate Parameterizations

A number of parameterizations have been developed that attempt to relate microscale dissipation to more easily measured finescale quantities. We can compare these schemes for self-consistency using this coastal California dataset. The Gregg (1989) parameterization involves the fourth moment of shear:

$$\langle \varepsilon_{IW} \rangle = 7 \times 10^{-10} \left\langle \frac{N^2}{N_o^2} \right\rangle \left\langle \frac{S_{10}^4}{S_{GM}^4} \right\rangle \quad \text{(W kg}^{-1}\text{)}, \quad \text{(E1)}$$

where $N_o = 0.0052$ s^{-1} (3 cph) is a reference buoyancy frequency, S_{10} is the shear having wavelengths greater than 10 m, and S_{GM} is the corresponding GM75 shear. Here N is the mean observed buoyancy frequency.

Another estimate of dissipation rate uses Dillon's (1982) observed $\overline{L}_o = 0.8\overline{L}_T$. Here ε_i is computed for each overturn i (of the 2227 overturns described in Table 1 ⦿) in terms of its rms Thorpe displacement L_T and local mean stratification N (computed from reordered density profile in the nonzero Thorpe displacement region):

$$\varepsilon_i = 0.64 L^2_{T_i} N^3_i. \qquad (E2)$$

Depth-mean dissipation rate is given by integrating over the volume V spanned by each profile (or, equivalently, by summing over the observed overturns in depth range sampled, H):

$$\langle \varepsilon_T \rangle = \frac{1}{V} \int_V \varepsilon \, dV = \frac{1}{H} \sum_i \varepsilon_i L_{P_i}, \qquad (E3)$$

where L_{P_i} is the patch size of the ith overturn.

Correspondence is observed between overturns and the presence of small-scale waves, indexed by the effective strain rate $\partial\hat{w}/\partial z$. To determine if this quantity is related to other dissipation rate estimates, an ad hoc scaling of depth-mean $(\partial\hat{w}/\partial z)^2$ is used to form a quantity whose magnitude and range of variation are comparable to those of observed ε_T:

$$\langle \varepsilon_{AP} \rangle = 500 \left\langle \left(\frac{\partial\hat{w}}{\partial z} \right)^2 \right\rangle^2 \qquad (E4)$$

(ε is in W kg^{-1}, and $(\partial\hat{w}/\partial z)^2$ is in s^{-2}).

Tables

Table 1. Experiment overturn summary. Properties of the 2227 overturns with $L_{max} \geq 2$ m found during the entire experiment (yeardays 59–68), between 200 and 350 m. The Thorpe scale L_T is the rms Thorpe displacement in the overturning region; L_{max} is the maximum Thorpe displacement and L_P is the vertical extent of the region, defined as the distance over which Σ (Th) $\neq 0$.

	Min	Max	Mean	Median
L_{max} (m)	2.15	36.92	4.40	3.38
L_P (m)	0.77	38.77	5.32	4.15
L_T (m)	0.97	15.91	2.38	1.88

Click on thumbnail for full-sized image.

Table 2. Twelve-hour overturn summary. Properties of the 330 overturns (a subset of those in Table 1) with $L_{max} \geq 2$ from yearday 67.5 to yearday 68.0, between 200 and 350 m.

	Min	Max	Mean	Median
L_{max} (m)	2.15	14.77	4.15	3.23
L_P (m)	1.23	15.69	4.93	3.85
L_T (m)	0.98	8.44	2.27	1.80

Click on thumbnail for full-sized image.

Table 3. Mixing estimates of mean kinetic energy dissipation rate $\overline{\varepsilon}$, corresponding dissipation Reynolds number [Eq. (9)], and eddy diffusivity $\overline{K}_\rho$ [Eq. (10) for yeardays 59–68, between 200 and 350 m. See appendix E for details.

Technique	$\overline{\varepsilon}$ (W kg^{-1})	Re $= \overline{\varepsilon}/\nu N^2$	$\overline{K}_\rho$ (m^2 s^{-1})
Gregg (1989)	6.81×10^{-9}	351	7.04×10^{-5}
Dillon (1982)	8.65×10^{-9}	447	8.94×10^{-5}

Click on thumbnail for full-sized image.

Figures
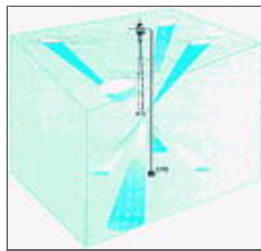
Fig. 1. Schematic diagram of CTD and Doppler sonar aboard *FLIP*.
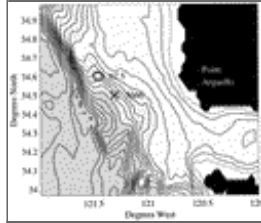
Fig. 2. Location of the Marine Boundary Layer Experiment (MBL). Bathymetry contours in meters (Sandwell and Smith 1997) are shown. The contour interval is 200 m, with 1000 m intervals indicated by increasing gray shading. *FLIP* was moored for the first portion of the experiment (black "×"). At UTC 66, the mooring line was severed. By UTC 67.5, *FLIP* had drifted to the position indicated by the black circle.
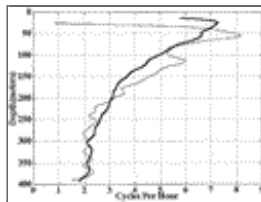
Fig. 3. MBL 9-day (solid line) and 12-h (yearday 67.5–68) mean (light line) buoyancy frequency profile.
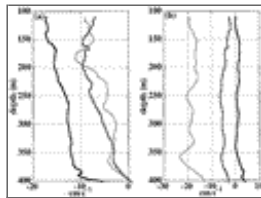
Fig. 4. MBL mean zonal (a) and meridional (b) currents. Averages are computed while moored (yearday 56–66, heavy solid line), while drifting (yearday 66–68, heavy dashed line), and for the 12-h period from yearday 67.5–68 (light line), which is featured in subsequent figures.
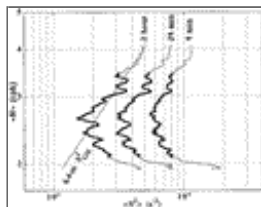
Fig. 5. Mean shear squared ($\overline{S^2}$) profiles are plotted vs 9-day mean buoyancy frequency $\overline{N}$ for depth ranges 150–400 m. The depth interval 200–350 m is indicated by the heavy lines. The rise in variance with depth below $\overline{N} = 2.75$ cph suggests a deep source of wave energy. All curves show $\overline{S^2} \sim \overline{N^2}$ above $\overline{N} = 2.75$ cph (250 m). The 4-min $\overline{S^2}$ is approximately twice Garrett–Munk (dotted line) for $\overline{N} \geq 2.75$ cph, above the zone of increased shear. It increases further with depth.
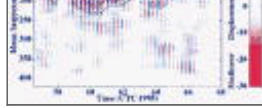
Fig. 6. Semi-Lagrangian depth–time map of tidal band [$1/(16\ h) \leqslant \omega \leqslant 1/(8\ h)$] isopycnal vertical displacement (color) and potential energy (contours), showing passage of a baroclinic tidal ray (yearday 60–62, 150 m). Displacements have been "WKB stretched" using the 9-day mean buoyancy profile (Fig. 3 ⬤⬤), by multiplying by $(\overline{N}(z)/N_o)^{1/2}$, where $N_o = 2.53$ cph is the 9-day mean value. Contours of potential energy $\rho_o N^2 \eta^2$ (where η is the isopycnal displacement) are 2, 4, 6, 8, 10 J m^{-3}.
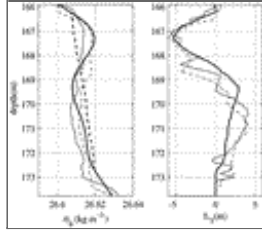
Fig. 7. (a) Full-resolution temperature (light solid line), conductivity (light dashed line), and 2-m density (heavy solid line) profiles for a sample overturn; T and C are expressed as equivalent densities $\rho_T = \alpha_T T + \beta_T$, $\rho_C = \alpha_C C + \beta_C$. The sorted density profile is plotted with a heavy dashed line. (b) Thorpe displacements computed from temperature (light solid line), conductivity (light dashed line), and density (heavy solid line). All three measures of L_T must be comparable before the inversion is considered an overturn.
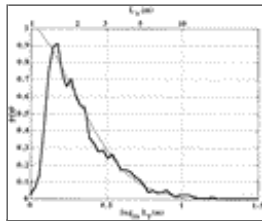
Fig. 8. Probability density function of log Thorpe scale, $\log_{10}(L_T)$, computed from all 2227 overturns (L_{max}) used in the study. To compute, data are binned into 51 bins spanning $0 \leqslant \log_{10}(L_T) \leqslant 1.5$. A reference Gaussian with $\sigma_{\log_{10}}(L_T) = 0.37$, $\overline{\log_{10}(L_T)}$ $= -0.1$ is overplotted (dashed line); L_T is approximately lognormal for $L_T \geq 1.5$ m.
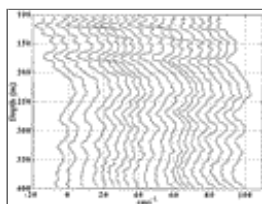
Fig. 9. Representative zonal velocity data (3.2-m vertical resolution) obtained from the MBL sonar. Twenty profiles (spanning 80 min) are plotted, offset by 5 cm s^{-1}. Adjacent profiles are averaged, resulting in independent estimates every 8 min.
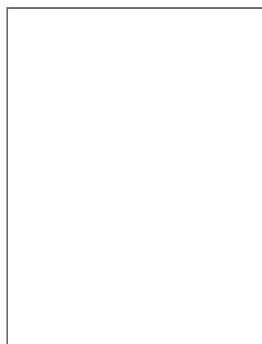
Fig. 10. Eulerian 2-m strain $\gamma_{Eul} = \overline{N^2}/N^2(z, t)$ (a), 6.4-m shear squared anomaly (b), and 6.4-m Ri $\equiv N^2/S^2$ (c) from yearday 1995 67.5–68.0 (12 h). Each has been averaged over 12 min (3 profiles) in time prior to plotting. Blue colors in (a) indicate lower than average buoyancy frequency; red colors in (b) indicate higher-than-average shear; red colors in (c) indicate low 6.4-m Ri. Yellow-green (a,b) and black (c) dots mark the locations of overturns whose maximum Thorpe displacement $L_{max} \geq 2$ m. Solid black lines are isopycnal depths (20-m mean spacing).
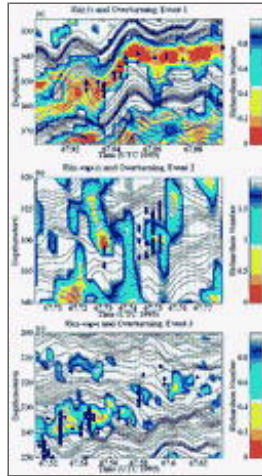
Fig. 11. Close-ups of individual events: 6.4-m Ri is contoured, and isopycnals (1-m mean spacing) and overturn locations are plotted for three events. Note the increased color scale in (b). In (b) and (c) the depth-mean has been removed at each time. Blue dotted lines indicate times of individual CTD drops, spaced 4 min apart.
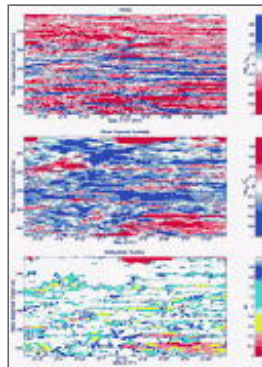
Fig. 12. Semi-Lagrangian strain, 6.4-m shear squared anomaly, and 6.4-m Ri, for the same depth range and period as in Fig. 10 ⊙. The ordinate specifies the isopycnal whose mean depth is indicated. Yellow–green (a,b) and black (c) dots indicate overturn locations. Solid black lines surround regions where Ri $\lesssim$ 1.
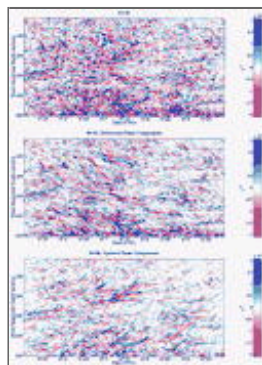
Fig. 13. Depth–time map of s-L effective strain rate $\partial\hat{W}/\partial z$ (a): $\partial\hat{W}/\partial z$ is computed from s-L γ using Eq. (7) and smoothing over two bins in time and two bins in depth. Wave propagation is more apparent when the field is separated into downward (b) and upward (c) propagating phase components. Yellow–green dots indicate overturn locations as in Fig. 12 ⊙.
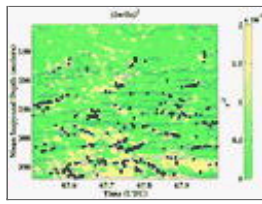
Fig. 14. Effective strain rate squared, $(\partial\hat{W}/\partial z)^2$. Data are smoothed over four isopycnals and 16 min in time, highlighting wave envelopes. Blue contours surround regions of Ri $\lesssim$ 1. Black dots indicate overturns as in Figs. 10–13 ⊙━.
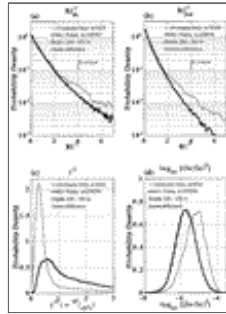
Fig. 15. Probability density functions of s-L Ri^{-1} (a), Eulerian Ri^{-1} (b), s-L γ^{-1} (c), and $\log_{10}(\partial\hat{W}/\partial z)^2$ (d). Heavy lines are computed using all observations from 200 to 350 m. Light lines represent observations at overturning regions. Overturning PDFs have been smoothed over $\Delta(\mathrm{Ri}^{-1}) = 0.25$, $\Delta(\gamma^{-1}) = 0.25$, and $\Delta(\log_{10}(\partial\hat{W}/\partial z)^2) = 0.20$, respectively. In (d), a Gaussian distribution with $\bar{y} = -5.67$, $\sigma = 0.56$ is plotted but completely obscured by the $(\partial\hat{W}/\partial z)^2$ curve.
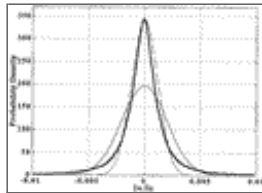
Fig. 16. Probability density function of effective strain rate $\partial\hat{W}/\partial z$ (heavy black line). Data are from the same time–depth range as in 15. Overplotted are reference Gaussians with same peak value (dashed line) and same variance (light black line) as the observed distribution.
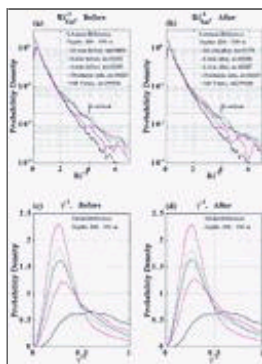
Fig. 17. Probability density functions of Eulerian Ri^{-1} (a, b) and s-L γ^{-1} (c, d) computed using data before (a, c), and after (b, d) observed overturning events. In each, the black line is computed using all data. The red line is computed using data at overturning locations. Magenta, blue, and green lines are computed using data 24, 8, and 4 min before/after observed overturns, respectively. Overturning and before/after PDFs have been smoothed as in Fig. 15 ⊙━.
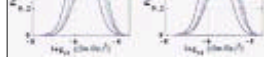
Fig. 18. Probability density functions of $\log_{10}(\partial\hat{W}/\partial z)$, computed using data before (a) and after (b) observed overturning events. Colors are the same as in Fig. 17 .
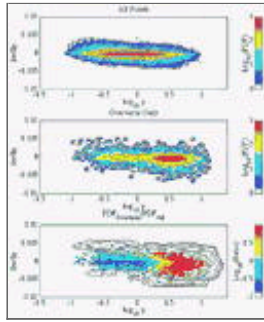
Fig. 19. Joint PDFs of $\partial\hat{W}/\partial z$ and $\log_{10}\gamma^{-1}$. The logarithm of the PDF is displayed, computed using all data (a) and overturning data only (b). The ratio is shown in (c) Data are binned in a 100 by 100 matrix, and histograms are then computed. The solid black lines are a smoothed version of the color contours. Values used are $\log_{10}(\text{PDF}) = \{0.5, 1, 1.5, 2, 2.5, 3, 3.5\}$ in (a, b) and $\log_{10}$ (ratio) $= \{0, \tfrac{1}{3}, \tfrac{2}{3}, 1\}$ in (c). Color contours in (b) and (c) have been smoothed with a convolution filter [3 bins by 3 bins in (b), 5 bins by 15 bins in (c)] before plotting.
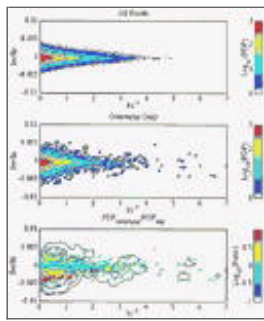
Fig. 20. Joint PDFs of $\partial\hat{W}/\partial z$ and s-L Ri^{-1}. As in Fig. 19 , the logarithm of the PDF, computed using all data, is shown in (a), overturning data only in (b). The ratio is shown in (c). The black contour levels (smoothed versions of the color contours) in (a) and (b) are the same as in 19. Levels in (c) are $\log_{10}(\text{ratio}) = \{0.15, 0.4, 0.8, 1.2\}$. Color contours in (b) and (c) have been smoothed with a convolution filter [3 bins by 3 bins in (b), 10 bins by 10 bins in (c)] before plotting.
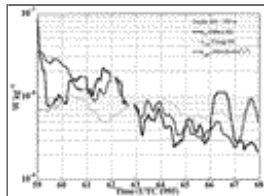
Fig. 21. Time series of inferred depth-averaged dissipation rate (appendix E), estimated from Thorpe scales (black line), 10-m shear (gray line) and $(\partial\hat{W}/\partial z)^2$ (dashed line). Each time series is computed using data from 200–350 m and is smoothed with a 16-h convolution filter prior to plotting. Extreme values appear in the filtered record as flat-topped features (e.g., black line, yearday 66.5).
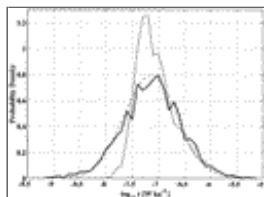
Fig. 22. Probability density of Thorpe-inferred dissipation $\mathcal{E}_T (= 0.64L_T^2 N^3)$ for all 2227 observed overturns with $L_{max} \geq 2$ m; $\mathcal{E}_T$ is approximately lognormal [dotted line, ($\overline{\log_{10} \mathcal{E}_T} = -7.15$, $\sigma_{\log_{10} \mathcal{E}} = 0.5$, "intermittency" factor $\sigma \ln^{\mathcal{E}} = 1.3$]. The PDF of $\mathcal{E}_T c \equiv \mathcal{E}_T \overline{N^2}/N^2$ is plotted with a light line.
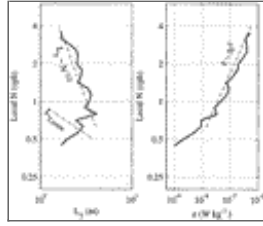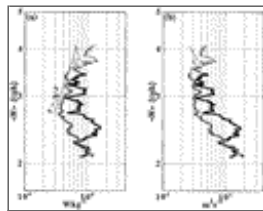

Click on thumbnail for full-sized image.

Fig. 23. Dependence of Thorpe scale L_T (a) and Thorpe-inferred dissipation $\mathcal{E}_T$ (b) upon instantaneous, local stratification N; L_T and $\mathcal{E}_T$ are averaged over all overturns whose mean buoyancy frequency (computed from sorted density profiles over the extent of the overturn) falls into the given range of N. For intermediate values of N, $L_T \sim N^{-1/2}$ and $\mathcal{E}_T \sim N^2$. Observed L_T is clearly not related to $L_{T,noise}$ (N) [Eq. (11), dash–dot line], the expected size of noise-generated density inversions.
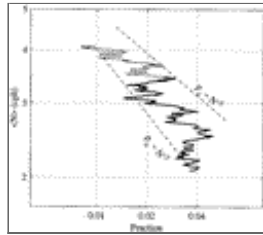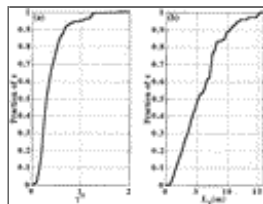

Click on thumbnail for full-sized image.

Fig. 24. Overturning fraction p_o $(\overline{N})$, where $\overline{N}$ is the mean Eulerian mean buoyancy frequency. The plotting scale is logarithmic on both axes. For depth ranges 200–350 m (heavy line) and the extended 150–200 m (light line), p_o $(\overline{N})$ scales approximately as $\overline{N}^{-3}, \overline{N}^{-2}$ (dashed lines). For $\overline{N}$ 2.5 cph, p_o appears constant.

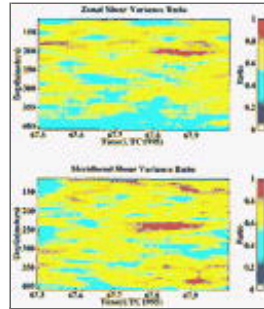Click on thumbnail for full-sized image.

Fig. 25. Mean dissipation rate $\mathcal{E}_{mean}$ $(\overline{N})$ (a) and diapycnal diffusivity $K_\rho(\overline{N})$ (b) computed from overturns [Dillon (1982), black lines] and from $(\overline{S^2})^2$ [Gregg (1989), gray lines]. Heavy lines correspond to the range 200–350 m, and light lines span a range extending upward to 150 m. Parameterizations in terms of overturns and shear demonstrate similar dependence upon $\overline{N}$ [$\mathcal{E}_{mean}(\overline{N})$ $\sim \overline{N}^2$ for $\overline{N} \geq 3$ cph]. High diapycnal diffusivities (b) are implied, which increase with depth.
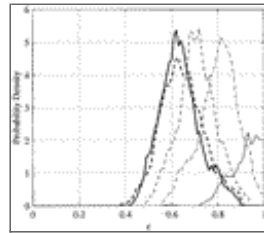

Click on thumbnail for full-sized image.

Fig. 26. Contributions to the 9-day mean Thorpe-inferred dissipation rate from overturns associated with inverse strain γ^{-1} (a) and Thorpe scale L_T (b); $C_\gamma{-1}(x)$ (a) and $C_{L_T}(x)$ (b) are plotted [Eqs. (13), (14)]. Each quantity $C(x)$ represents the fraction of total

dissipation accounted for by all overturns with $\gamma^{-1} \lesssim x$ (a) or $L_T \lesssim x$ (b). From (a), 95% of dissipation results from weaker-than-average stratification ($\gamma^{-1} \lesssim 1$). From (b), overturns of all sizes contribute comparably to dissipation, for $L_T \lesssim 8$ m. "Big bangs" ($L_T \gtrsim 10$ m) contribute less than 10% of total.
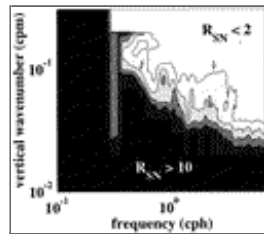

Click on thumbnail for full-sized image.

Fig. A1. The ratio $\hat{r}(z, t)$ of Janus average shear variance to the maximum of the variance in the two constituent beams [Eq. (A7)], for zonal (a) and meridional (b) shear, for the same period considered elsewhere. For plotting only, averages are computed over 20 m in depth and 2 h in time; $1 - \hat{r}$ is an upper bound on the fraction of shear variance unresolved due to beam separation effects. It includes contributions from the true strain rate, $\partial w/\partial z$.
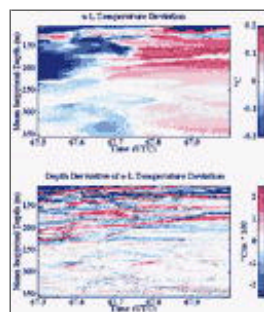

Click on thumbnail for full-sized image.

Fig. A2. Probability density function of $\hat{r}$ estimated from zonal shears (heavy solid line) and meridional shears (heavy dashed line). Data from 200 to 350 m, yearday 67.5–68.0 ($\sim$ 18 000 data) are used in the calculation. Both estimates have $\lesssim 4\%$ probabilities of $\hat{r} \lesssim 0.5$. Light lines are PDFs of $\hat{r}'$ [Eq. (A7)], computed with mean $|\partial \hat{w}/\partial z| = \frac{1}{4}$ (light dashed line), $\frac{1}{2}$ (light dash–dot line), and 1 (light solid line) times the 9-day mean value of 1.73×10^{-6} s^{-2}.
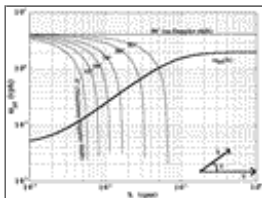

Click on thumbnail for full-sized image.

Fig. A3. Signal to noise ratio $S_N(\omega, m)$ is computed by attributing to noise the difference between vertical velocity estimates made from the two different back-to-back beam pairs. It is a conservative lower bound, as true spatial variability between the beams is considered as noise. Darker regions (low wavenumber and frequency) display $S_N(\omega, m) \geq 10$. Lighter regions high wavenumber and frequency) have $S_N(\omega, m) \lesssim 2$; $S_N \geq 2$ at 10-m scales with $\sim$ 1 h averaging.

Click on thumbnail for full-sized image.

Fig. C1. Semi-Lagrangian temperature anomaly (a) and its depth derivative (b). Temperature fluctuations along isopycnals relative to a 12-h time mean are displayed. Intrusive activity and frontal interleaving is seen. Variability in these plots cannot be due to straining by internal waves.

Click on thumbnail for full-sized image.

Fig. D1. Equation (D1) (light black lines) and (D2) (heavy black line) are plotted vs horizontal wavenumber. Different light lines refer to different assumed angles (0, 45, 60, 70, 80, 85, 90) between wave vector $\mathbf{k}$ and advective velocity $\mathbf{U}$. Assumed values are $U = 0.2$ m s^{-1}, $m = 0.08$ cpm, $N = 2$ cph, $f = 1/24$ cph, $\omega_{obs} = 4$ cph. Intersections correspond to inferred values of k, ω_{int} consistent with linear internal waves Doppler shifted by the indicated amount.

[1] The Ri-based parameterization ε_{KWB} of Kunze et al. (1990) appears to track ε_{IW} quite well. Its magnitude is ad hoc due to uncertainties in which differencing scale and critical Ri value are appropriate (Polzin et al. 1995).

Corresponding author address: Dr. Matthew H. Alford, Ocean Physics Department, Applied Physics Laboratory, University of Washington, 1013 NE 40th St., Seattle, WA 98105-6698.

E-mail: malford@apl.washington.edu

top ▲